Charles University in Prague
Faculty of Mathematics and Physics

MASTER'S THESIS

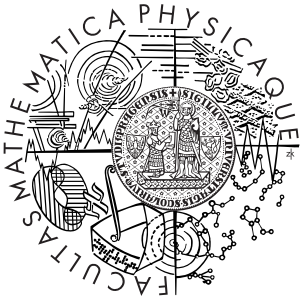

Daniel Scheirich

Development of Optimal Algorithms for the Selection of Rare Semimuonic B Decays in ATLAS

Institute of Particle and Nuclear Physics

Supervisor:	Zdeněk Doležal
Co-supervisor:	Mária Smižanská[1]
Study programme:	Physics
Study field:	Nuclear and Subnuclear Physics

2008

[1] Lancaster University, UK

Karlova univerzita v Praze
Fakulta matematicko-fyzikální

DIPLOMOVÁ PRÁCE

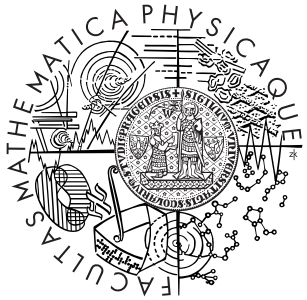

Daniel Scheirich

Vývoj optimálních algoritmů pro selekci řídkých semimionových B rozpadů v detektoru ATLAS

Ústav částicové a jaderné fyziky

Vedoucí práce:	Doc. RNDr. Zdeněk Doležal, Dr.
Konzultant:	Mária Smižanská, Ph.D.[1]
Studijní program:	Fyzika
Obor:	Jaderná a subjaderná fyzika

2008

[1]Lancaster University, UK

Acknowledgement: I would like to thank my supervisors Zdeněk Doležal and Mária Smižanská for their valuable advice and appreciated comments, as well as Takanori Kono and Hiro Kyiamura for helping me with a development of the muon trigger calibration method. Last but not least I would like to thank Pavel Řezníček, whose expertise on semimuonic rare B decays proved to be very helpful.

I declare that I wrote my master's thesis independently and exclusively with the use of the cited sources. I agree with lending and publishing the thesis.

Prohlašuji, že jsem svou diplomovou práci napsal samostatně a výhradně s použitím citovaných pramenů. Souhlasím se zapůjčováním práce a jejím zveřejňováním.

In Prague, Apr 16, 2008 Daniel Scheirich

Contents

Title: Development of Optimal Algorithms for the Selection of Rare Semimuonic B Decays in ATLAS
Author: Daniel Scheirich
Department: Institute of Particle and Nuclear Physics
Supervisor: Zdeněk Doležal
Supervisor's e-mail address: dolezal@ipnp.troja.mff.cuni.cz

Abstract: In this thesis we propose the trigger algorithm for the semimuonic rare B decay selection in ATLAS experiment and we study its performance using the Monte Carlo sample of $\Lambda_b \to \Lambda^0 \mu^+ \mu^-$. The cut optimisation have been performed in order to obtain the optimal cut values and the signal rate for the process was estimated. The feasibility and performance of the tag-and-probe method for the calibration of di-muon triggers is investigated, too. Effects of the systematic uncertainties of the method on the measurements of J/ψ polarisation and the forward-backward asymmetry of $\Lambda_b \to \Lambda^0 \mu^+ \mu^-$ were studied.

Keywords: ATLAS, rare B decays, level-2 trigger, efficiency calibration, tag-and-probe method

Název práce: Vývoj optimálních algoritmů pro selekci řídkých semimionových B rozpadů v detektoru ATLAS
Autor: Daniel Scheirich
Katedra (ústav): Ústav částicové a jaderné fyziky
Vedoucí práce: Zdeněk Doležal
E-mail vedoucího: dolezal@ipnp.troja.mff.cuni.cz

Abstrakt: V této práci navrhujeme algoritmus pro trigger selekci vzácných B rozpadů v experimentu ATLAS a studujeme jeho vlastnosti pomocí $\Lambda_b \to \Lambda^0 \mu^+ \mu^-$ Monte Carlo souboru. Provedli jsme optimalizaci selekčních prahů za účelem získání nejlepších hodnot a spočetli jsme frekvenci nabírání signálních případů. Rovněž studujeme možnost využití a vlastnosti tag-and-probe metody pro kalibraci dvou-mionových triggerů. Byl vyšetřován vliv systematických chyb metody na měření J/ψ polarizace a předo-zadní asymetrie v $\Lambda_b \to \Lambda^0 \mu^+ \mu^-$.

Klíčová slova: ATLAS, vzácné B rozpady, trigger druhé úrovně, kalibrace účinnosti, tag-and-probe metoda

Chapter 1

Introduction

Semimuonic rare B decays represent one of the physics channels that will be measured at ATLAS experiment. Since they are tree-level forbidden in the standard model, they make a good testing ground for the standard model predictions and allow to observe some signatures of a potential new physics. The new physics effects could be seen in the shape of the forward-backward asymmetry with an advantage that a lot of hadronic uncertainties cancel in the definition of the quantity. Considering low branching ratios of the decays, a good trigger and offline selection is required in order to suppress the rate of background processes which is several orders of magnitude higher than the signal one.

The thesis is divided into eight chapters. In Chapters 2 and 3 we present a general overview of the ATLAS detector and its trigger system, respectively. A brief description of several trigger algorithms that we use in this thesis can be found here. Chapter 4 explains a theoretical framework used for the description of the rare B decays and defines an experimentally measured quantity – the forward-backward asymmetry. It also presents some basic concepts and methods of the offline reconstruction and analysis of the studied processes.

The author's work is concentrated in Chapters 6 and 7. In Chapter 6 of this thesis we propose a trigger algorithm that is designed to select the semimuonic rare B decays at ATLAS. Its performance is studied using Monte Carlo samples of $\Lambda_b \to \Lambda^0 \mu^+ \mu^-$ process. We investigate several settings of the algorithm and we have performed a cut optimisation in order to achieve the optimal performance. For LHC luminosity run of 10^{33} cm^{-2}s^{-1} signal and background rates were estimated. In addition, the rates were estimated also for the luminosity of 10^{34} cm^{-2}s^{-1} even though at a present time it is not decided whether there will be a b-physics program for that LHC run.

Since an important part of the algorithm consists of a di-muon trigger, we devote Chapter 7 to the muon trigger calibration. The tag-and-probe calibration method is studied using Monte Carlo samples of $J/\psi \to \mu^+ \mu^-$ process and we discuss its use for di-muon triggers. The systematic uncertainties of the method are studied on J/ψ events as well as events with $\Lambda_b \to \Lambda^0 \mu^+ \mu^-$ process. We show that the systematic errors of the calibration don't affect the shape of the

forward-backward asymmetry.

Results of the studies are going to be published in CERN publications [9] and [11]. The rare decays part will be presented in the latter reference, while the study on the trigger calibration is going to be published in the first one. In this thesis, we do not cite the references in cases when we present the author's results. However, we cite them whenever we refer to the other parts of the publications.

In the whole thesis we use the *system of natural units* ($h = c = 1$) when we present values of energy, mass and momentum. It means that all the mentioned quantities are in GeV.

Chapter 2

ATLAS Experiment

ATLAS (A Toroidal LHC ApparatuS) [1] is one of the four main experiments at the *Large Hadron Collider* (LHC). At present time, LHC is being build at Centre Européenn pour la Recherche Nucléaire (CERN, European Centre for Nuclear Research) in Geneva, Switzerland. LHC will collide proton–proton beams with energy of 14 TeV per a single collision (7 TeV + 7 TeV) and expected nominal luminosity of 10^{34} cm^{-2}s^{-1}. There are four interaction points at the collider circumference and each of them is occupied by one of the main experiments: ATLAS, LHCb, CMS and ALICE.

The ATLAS experiment is designed to exploit a full discovery potential of LHC. The ATLAS physics programme focuses mainly on the origin of mass at electroweak scale based on a spontaneous symmetry breaking, which can manifest itself by an existence of the standard model Higgs boson, a family of Higgs particles or a strongly interacting Higgs system. Searches for heavy W and Z-like objects predicted by super-symmetry (SUSY) and other beyond-standard model theories, as well as searches for exotic physics signatures like black holes, extra dimensions and gravitons represent another goal of the experiment. We must also mention a high rate of b and t-quarks which makes LHC a powerfull b-factory. It allow physicists to study properties of B hadrons including a general spectroscopy of B-states, their production mechanisms, precise measurements of CP violation and determination of elements of Cabbibo-Kobaiashi-Maskawa matrix (CKM).

The above mentioned measurements require a very good electromagnetic calorimetry for a photon and electron identification. A hadronic calorimeter must provide accurate measurements of jets and a good η and full ϕ coverage is necessary for precise missing transverse energy measurements. A muon spectrometer together with an inner detector tracking must be able to accurately measure low-p_{T} muons with a possibility to measure high-p_{T} muons with the spectrometer alone. The tracking is required to be efficient for high-p_{T} lepton-momentum measurements, an electron and photon identification and τ-lepton and heavy-flavour identification. A full event reconstruction capability is necessary for the low luminosity run. A triggering and measurements of particles must be done with low-p_{T} thresholds, providing high efficiencies for most physics processes of

interest at LHC [1].

A layout of the detector system is shown in Figure 2.1. It consists of the following subdetectors: the inner detector, the electromagnetic and hadronic calorimeter and the muon spectrometer. The magnet system consists of a thin solenoid placed at the outer radius of the inner detector and air core toroids in the muon spectrometer outside of the hadronic calorimeter.

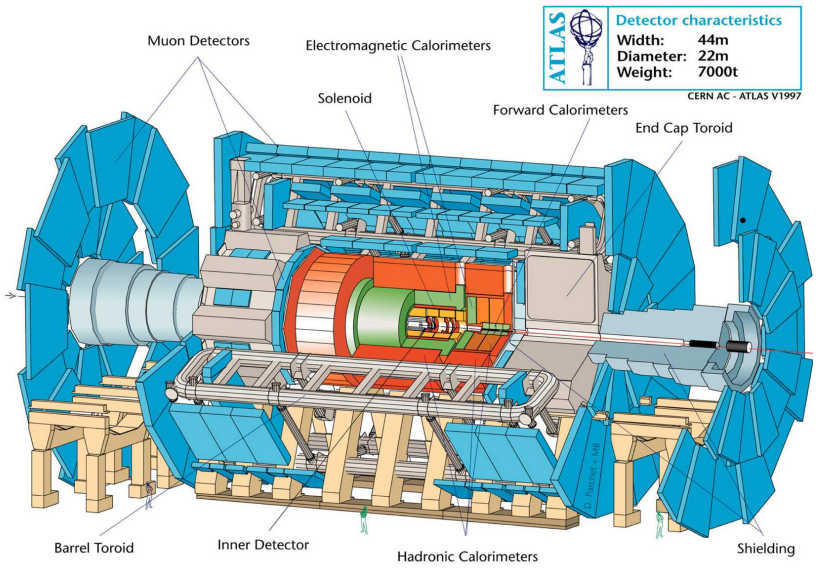

Figure 2.1: ATLAS experiment.

The superconducting solenoid is 5.3 m long with a diameter of 2.44 m and provides a magnetic field of 2 T for precise momentum measurements in the inner detector. It shares its cryostat with the liquid-argon (LAr) electromagnetic calorimeter. There are three toroid magnets, one barrel toroid and two end-cap toroids. Each of them consists of eight independent superconducting coils arranged with an eight-fold symmetry. The outer and inner diameter of the barrel toroid is 20.1 m and 9.4 m respectively and it is 25.3 m long. Two end-cap toroids enclose the magnet system from sides and they have an outer diameter of 10.7 m. The toroid magnets provide a magnetic field for p_{T} measurements in the muon system that is independent on the inner detector. The magnetic field of the toroids is not homogeneous and its peak value is 3.9 T and 4.1 T for the barrel and the endcap toroids respectively.

The inner detector [4] is contained in the cavity of the electromagnetic calorimeter. It is 7 m long with a radius of 1.15 m. A pattern recognition, accurate momentum and vertex measurements and electron identification are achieved with a combination of discrete high-resolution silicon pixel and strip detectors in the inner part of the tracking volume, and continuous straw-tube tracking detectors with transition radiation capability in its outer part.

The silicon detectors are arranged in cylindrical layers parallel to the beam axis in the barrel region and perpendicular discs in the endcap regions. Each layer consists of a number of detector modules with an independent read-out electronics. For the purpose of the vertex measurements a high granularity around the interaction point is achieved by using a pixel technology [4]. The pixel detectors form three layers in the barrel region and five end-cap discs on each side. The semi-conductor tracker (SCT) [4] made of four barrel layers and nine end-cap discs on each side provides a precise measurement of track space-points. A silicon micro-strip technology was used in order to minimise cost and the number of read-out channels. The strip detectors allow to measure position only in one dimension (perpendicular to the strips). The two-dimensional position measurement in each module was achieved by using two silicon wafers that are rotetad by an angle of 40 mrad.

The transition-radiation tracker (TRT) represents the outermost part of the inner detector. TRT straws are laid in parallel to the beam in the barrel region and in radial in the end-caps. Two thresholds on the charge deposited in the straws – which is proportional to an intensity of a transition radiation – allow to distinguish between electrons and hadrons.

Typically, three pixel layers and eight strip layers (four space points) are crossed by each track. A large number of tracking points (typically 36 per track) is provided by TRT.

The highly granular LAr electromagnetic calorimeter [5] provides measurements of energy and an identification of photons, electrons and τ-leptons with an excellent performance. It covers a pseudorapidity of $|\eta| < 4.9$ and it is hermetic in ϕ. LAr technology is also used for the hadronic calorimeter in end-caps. However, the bulk of the hadronic calorimetry is provided by a scintillator-tile calorimeter (TileCal), which is separated into a large barrel and two smaller extended barrel cylinders, one on each side of the barrel. Both calorimeters are contained in a cylinder with a radius of 4.25 m and a width of 12.2 m.

A layout of the muon system [6] is shown in Figure 2.2. Four types of muon detectors are used. In the barrel, *resistive plate chambers* (RPC's) are used for the trigger and *monitored drift tube chambers* (MDT's) for an accurate tracking. In the end-caps, *thin gap chambers* (TGC's) are used for the trigger, MDT and *cathode strip chambers* (CSC's) for the tracking.

A momentum measurement is based on a deflection of muon trajectories in the magnetic fields of three air-core toroids. In a pseudorapidity region $|\eta| < 1$ the tracks are bent by the field of the barrel toroid. For a pseudorapidity $1.4 < |\eta| < 2.7$ the deflection is provided by the end-cap toroids. A region of $1.0 < |\eta| < 1.4$ is so called *transition region* and here the deflection is provided by a combination of the barrel and end-cap fields. The magnet configuration provides a field that is mostly orthogonal to the muon trajectories.

In the barrel region, the muon chambers are arranged to three *super-layers* or so called *stations*. Each super-layer consists of six or eight layers of the monitored drift tubes. The stations are placed near inner and outer field boundaries and

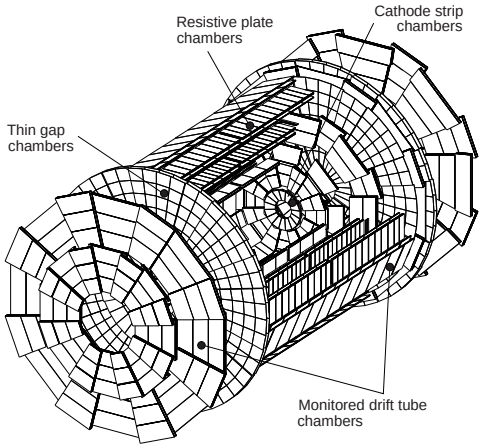

Figure 2.2: layout of the muon chambers [6].

inside the field volume in concentric cylinders with radii of about 5, 7.5 and 10 m. They cover a pseudorapidity of $|\eta| < 1$. A momentum is determined from the measurement of a sagita of the track.

In the transition and the end-cap regions, the cambers are arranged to four discs orthogonal to the beam axis placed in distances of 7, 10, 14 and 21–23 m from the interaction point. Cryostats of the end-cap toroids don't allow to place chambers inside the magnetic field. Therefore the momentum is determined with the highest possible resolution from a point-angle measurement.

Both in the barrel and the end-caps the chambers are arranged in a sixteen-fold symmetry while the magnetic field have an eight-fold symmetry reflecting the position of the toroid coils. Over the most of the pseudorapidity range the high-precision tracking is provided by MDT chambers. At a large pseudorapidity close to the beam axis CSC's are used to sustain high radiation conditions. In the barrel region two MDT chambers at the bottom side have a special shape because of the rails supporting the calorimeters. Chambers at the pseudorapidity of $\eta = 0$ are missing to make space for cables.

The muon trigger system covers a pseudorapidity range of $|\eta| < 2.4$. In the barrel, RPC's are placed in three layers: on both sides of the middle MDT chamber station and directly below or above the outer one. TGC's are located near the middle station of the end-caps.

Chapter 3

ATLAS Trigger System

At LHC the proton bunches will cross at a frequency of 40 MHz which correspond to a period of 25 ns [1]. With approximately 1 Mbyte per event at the nominal luminosity of 10^{34} cm^{-2} s^{-1} it would give a data flow of 4×10^7 Mbyte s^{-1} if all the events were stored. It is evident that such a flow is too large to be handled by a present-day hardware. Also, most of the events don't contain any interesting physics processes thus there is no need to store them. It is essential that the events are filtered and the rate of the permanently stored events is lowered to a manageable level. Reduction of the event rate is provided by so called *trigger system*. The trigger system must be able to reduce the event rate while preserving events with signatures of an interesting physics (e.g. Higgs boson, super-symmetric particles, etc.) It performs a fast analysis of the event and decides whether to keep or to reject it. This way the ATLAS trigger system reduces the rate by order of 10^7 from initial 40 MHz to about 100 Hz [1] that can be stored on tapes. An available processing time at each trigger level together with the output rate is shown in Figure 3.1.

Another challenge of the trigger system is to associate each reconstructed object with the corresponding bunch crossing. Because of the extended size of the muon spectrometer, time-of-flight of muons is the same order of magnitude as the time period between two bunch crossings.

ATLAS trigger system has three levels: *Level-1* [3], *Level-2* and *Event Filter*. The latter two are also known under a common name *High-Level Trigger* (HLT) [2]. Each level refines the decision made by the previous one and adds an additional selection criteria where necessary.

3.1 Level-1 trigger

The level-1 trigger is entirely hardware based and it uses only a subset of ATLAS detectors in order to increase a decision speed. High p_{T} muons (with $p_{\mathrm{T}} \geq 4$ GeV at the initial run and $p_{\mathrm{T}} \geq 6$ GeV at the nominal luminosity) are reconstructed using only RPC's and TGC's. In both electromagnetic and hadronic calorimeters

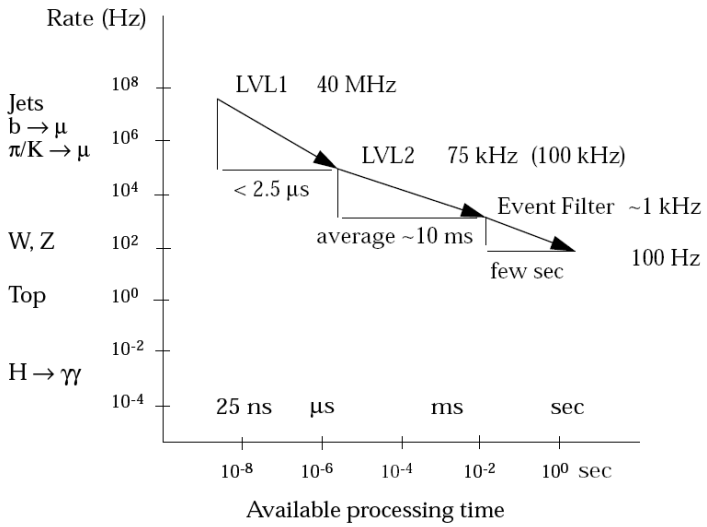

Figure 3.1: Available processing time vs. output rates of three trigger layers [1].

the reduced granularity is used for an event selection. No information from the inner detector is available at level-1.

The level-1 trigger uses simple algorithms to make a decision. The algorithms are executed by a custom electronics with adjustable parameters. They reduce the initial event rate down to 75 kHz (upgradable to 100 kHz) [3]. The execution time of the level-1 decision is about 2 μs. Before a decision is made, data from all of the $\sim 10^7$ ATLAS detector channels are stored in *pipeline memories* waiting to be read out in case the event was accepted. Data are then moved from the pipelines to *read-out buffers* from which they are accessible by level-2 trigger processors. According to estimates of the interesting physics processes rate [1], an available level-1 output rate is higher by a safety margin of two. This is not over-generous since there are huge uncertainties in the rate estimates.

The level-1 trigger creates several types of *trigger objects* and each object contains information about selection thresholds it has passed as well as the information about its position (η and ϕ coordinates). The level-1 trigger decision is then based on the combination of the objects required in the coincidence or veto. The level-2 trigger algorithms are usually based on *regions of interest* (RoI's) provided by level-1. It means that only a small portion of information from the window around accepted level-1 trigger objects is passed to level-2 algorithms. This significantly reduces the execution time of the level-2 algorithms since only a small fraction of the event is transferred to the level-2 processors.

The list of the level-1 trigger objects follows:

Muon RoI: muon candidate object reconstructed by the ATLAS muon spectrometer. The level-1 muon trigger provides six independently programmable p_{T} thresholds. There are two sets of thresholds available, one for the

initial luminosity run with the thresholds of 4 GeV, 6 GeV, 8 GeV (low p_{T} thresholds), 11 GeV, 20 GeV and 40 GeV (high p_{T} thresholds); and the other set for the nominal luminosity run with the thresholds of 6 GeV, 8 GeV, 10 GeV (low p_{T} thresholds), 11 GeV, 20 GeV and 40 GeV (high p_{T} thresholds). More details on the level-1 muon trigger is going to be given in Chapter 3.4.1.

EM/Tau RoI: electron, photon or τ-lepton candidate reconstructed by the ATLAS electromagnetic calorimeter. Electrons and photons create a shower in electromagnetic calorimeter with the same shape and thus are indistinguishable by the level-1 trigger (EM candidates). τ-leptons decayed into a hadronic final state create a narrow jet of pions which makes a signal in the electromagnetic and also in the hadronic calorimeter. 16 E_{T} thresholds as well as criteria on isolation (both EM and τ candidates) and hadronic veto (EM candidates) can be applied on EM/τ objects. The first 8 thresholds must be EM and the other 8 may be EM or τ.

Jet RoI: hadronic jet candidate reconstructed by hadronic calorimeter. Two different sets of E_{T} thresholds are available for central and forward jets. 8 for central and 4 for forward jets.

Missing E_{T}: signature of neutral weakly interacting particles. E_{T} of all reconstructed jets (or jets with E_{T} above some optional threshold) is converted to E_x and E_y using their ϕ coordinate which are then summed. Set of 8 thresholds can be applied on the global sum.

Total E_{T}: total transverse energy calculated as a sum of E_{T} of all jets (or jets with E_{T} above some optional threshold). 4 thresholds can be applied on total energy sum.

Since this thesis focuses on trigger algorithms based on the muon trigger we won't go through the details of the calorimetric level-1 triggers. For more information on these triggers we refer the reader to [3].

3.2 Level-2 trigger

The high level trigger must reduce the rate coming from level-1 to about 100 Hz where most of the reduction is expected to be done by the level-2 trigger. Level-2 algorithms are RoI seeded thus only a small portion of the event is transferred to the level-2 trigger processors.

The processing steps of the level-2 trigger are as follows. The raw data associated to RoI's are collected and prepared. *Feature extraction* algorithms (FEX) are executed on the data. The feature extraction algorithms reconstruct the trigger objects – so called *features* – using the information from the ATLAS subdetectors. The features are for instance inner detectors tracks, calorimeter clusters or muon

spectrometer tracks and they are used to immediately confirm the level-1 RoI by which they were seeded. These objects are then combined to create identified level-2 physics object candidates such as muons, electrons, photons, τ's and jets, as well as generalised missing transverse energy and b-physics objects.

The identified physics objects are then passed to the *hypothesis algorithms* which perform a fast analysis and identify the physics processes. For instance two opposite-charged muon candidates are combined and the cut on their invariant mass is applied in order to select events with J/ψ particle decaying into muons.

According to [1] an average processing time of about 10 ms per event is assumed for the level-2 trigger. The feature extraction algorithms are at the heart of the level-2 trigger processing. The data transfer is also time consuming however the bulk of the algorithmic complexity lies in the feature extraction. The hypothesis algorithms are expected to be relatively simple. An exception is formed by b-physics hypothesis algorithms, because of rather complicated topologies of studied processes.

For b-physics, the most important feature extraction algorithms are those performing the muon reconstruction (see Chapter 3.4.2) and those performing an inner detector tracking. There are two main tracking algorithms available at level-2 – IDSCAN and SiTrack. We won't present any details on SiTrack algorithm since in this thesis we use only IDSCAN.

IDSCAN [7] performs a pattern recognition in the silicon trackers using space points. Then it uses Kalman filtering to fit the track. It can also extrapolate to the transition radiation tracker (TRT). The space points from the inner detector region around the level-1 RoI are passed to the algorithm. The size of the window is different for different settings of the algorithms. For instance the standard b-physics setting (IDSCAN_Bphysics) have the window with the size $\Delta\eta \times \Delta\phi = 1.5 \times 1.5$.

The reconstruction procedure consists of four steps: a reconstruction of the z-position of the primary pp collision (*zFinder*), the main pattern recognition step (*hitFilter* and *groupCleaner*), a final track fit and removal of outliers (*trackFitter*) and an extrapolation to TRT (*TRT extension*).

In the first step, the window is divided into number of ϕ slices. In every slice each pair of the points from different layers is used to calculate z by linear extrapolation to the beam axis. This assumes a solenoidal magnetic field, where the helix trajectories of charged tracks are straight lines in the $\rho - z$ projection. The histogram is filled with the calculated values and the bin with the most entries is taken as a z-position of the physics event.

In the next step groups of the points that belong to a single track with a high probability are created. The algorithm uses the fact that all the points of the single track has the same η with respect to the z-position of the physics process. A two-dimensional histogram in $\eta \times \phi$ is filled with the points coordinates and the points in the bin with the number of entries above a certain threshold are taken as a group. The size of ϕ bin determines the minimal p_{T} of the track that can be efficiently reconstructed by IDSCAN. The group is then cleaned, exploiting

the fact that from each three points of the track one can calculate the track parameters – a transverse momentum p_{T}, a transverse impact parameter a_0 and a direction at the perigee of the track ϕ_0. All the triplets with the similar p_{T} and ϕ_0 form a track candidate.

Finally the track candidates are passed to a fitter that employs extended Kalman filter and estimates the track parameters at the perigee of the track. The initial values of the parameters are taken from the previous step. The fitter calculates an expected χ^2 contribution in each point and remove the points with large χ^2. Corrections due to material effects are taken into account but a homogeneous magnetic field is used.

The track can be extrapolated to TRT subdetector using probabilistic data association algorithm.

Again, as in the case of level-1 trigger, we won't present any details about calorimetric triggers and turn our attention to the muon trigger. For the details on other triggers see [2].

3.3 Event Filter

Event filter represents the last level of the trigger selection. It has already access to the whole event and it uses complex algorithms with the performace similar to the one of the offline algorithms. Even though it can use the whole event, the event filter algorithms are guided by the level-2 objects similarly as level-2 algorithms are seeded by level-1. The task of the event filter is to perform the final selection and reduce the output rate from level-2 to approximately 100 Hz which is going to be stored.

3.4 Muon Trigger

3.4.1 Level-1 Muon Trigger

Level-1 muon trigger is based on a measurement of muon trajectories in three different planes (called stations). Because of the toroidal magnetic field the trajectory is deflected from the straight line and the angle of deflection is proportional to the muon momentum and integral of the magnetic field along the trajectory.

In the endcap, the trigger station farthest from the interaction point is called the *pivot plane*. In the barrel region, the pivot plane is the nearest trigger station. The muon originated in the nominal interaction point will ideally make hits in two or three trigger stations. Two different lever arms from the pivot plane to the other two stations provide two different measurements of the muon deflection due to the magnetic field. These two lever arms allow trigger thresholds to cover a wide range of transverse momenta with a reasonably good resolution. The shorter lever arm (pivot plane and station 2) covers a lower-momentum range and the longer one (pivot plane and station 1 for the end-cap, pivot plane and station 3

for the barrel) covers a higher-momentum range. The momentum measurement is schematically illustrated in Figure 3.2.

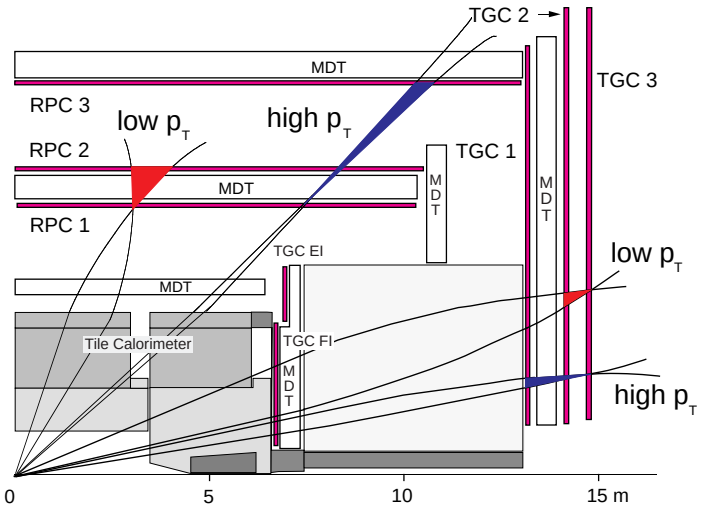

Figure 3.2: Level-1 muon trigger scheme [1].

The hit in the pivot plane is extrapolated along a straight line through the nominal interaction point to the other two stations. The coincidence window with size dependent on p_{T} threshold is then defined around these points. The muon is considered to pass the low-p_{T} threshold if there are hits in pivot plane as well as in the coincidence window of the low-p_{T} station. For high-p_{T} thresholds the coincidence is required between the pivot plane and the high-p_{T} stations and the muon must pass the low-p_{T} criteria too. In reality, the situation is slightly more complicated since the position of the points is measured independently for η and ϕ projection and not all the hits in all projections are required to be in the coincidence. For details see [3].

The size of the window defines p_{T} threshold – the wider the window, the lower the threshold. The windows are defined such that the efficiency at threshold is about 90%. A tight time coincidence among hits is also required, to identify the bunch crossing. The muon spectrometer is divided into regions in $\eta \times \phi$ where independent trigger windows can be used. The level-1 algorithm treats the overlaps between the sectors using the look-up-tables.

3.4.2 Level-2 Muon Trigger

A purpose of the level-2 muon trigger is the identification of the muon tracks, confirmation of the level-1 RoI, an accurate calculation of the position and transverse momentum in the muon spectrometer and an extrapolation to the calorimeter and the inner detector. The same as for the level-1 RoI's a cut on the level-2 muon candidate p_{T} can be applied.

The main level-2 algorithm is *MuFast* [8, 27]. It uses the full granularity of the muon detectors within the RoI. MuFast processes the data in three sequential steps: a pattern recognition involving level-1 trigger chamber hits and the position of the MDT hit tubes, a track fit performed on each MDT chamber, and p_{T} estimate using look-up-tables (LUT's) in order to avoid time consuming fitting methods.

Because a relatively high occupancy of MDT detectors is expected, it is necessary to select groups of MDT hits that were with a high probability caused by the muon triggered by level-1. This is done in the pattern recognition phase of MuFast algorithm. The trajectory of the muon is calculated using the level-1 hits and the assumption that the muon originated in the nominal interaction point. An area around this trajectory – so called *muon road* – is laid out and only the hit tubes that are inside the area are used as it is shown in Figure 3.3. The width of the muon road depends on the position and it is different for low-p_{T} and high-p_{T} muons. Finally a contiguity algorithm is applied on the selected hits in order to remove the background. This is a recursive procedure in which the mean direction of the hit cluster is computed and the hit tube having the highest deviation from the mean is removed. The contiguity algorithm terminates only when at most a single hit tube on each MDT layer is left.

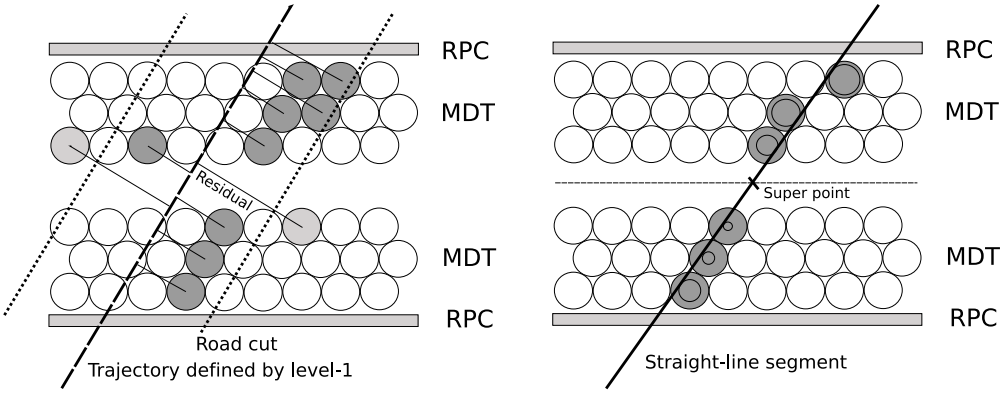

Figure 3.3: Muon road cut (left) and the straight line segment fit (right) of the MuFast algorithm [27].

In the second step, the trajectory of the muon is approximated by the straight line segments that are fitted in each MDT chamber (see Figure 3.3). An advantage of this approach is that a linear fit has an analytical solution therefore it is very fast while a complete helix fit through the spectrometer would require a time consuming minimisation procedure. Each segment provides an accurate position – so called *super point* – which is an intersect of the segment and the plane in the middle of the chamber. These super points are used to determine the trajectory bending in the magnetic field. Fake level-1 muons are rejected by requiring at least two super points for each RoI.

An estimate of the transverse momentum is done from the measurement of the track bending. The curvature radius R_c is calculated using three or two super points. In the latter situation the muon is assumed to be coming from the nominal interaction point. The transverse momentum is then approximated by the linear expression:

$$p_T = A_0 R_c + A_1. \tag{3.1}$$

p_T is proportional to the curvature radius and it depends on the integral of the magnetic field along the trajectory (contained in the parameter A_0). Since p_T in the interaction point is needed, the energy loss in the calorimeter must be taken into account, too (parameter A_1). The parameters A_0 and A_1 were calculated for differend $\eta \times \phi$ regions and are stored in the look-up-table.

In the standard trigger chain, muon candidates reconstructed by MuFast algorithm are then confirmed by the inner detector. An algorithm doing that is called *MuComb* [8, 28]. It receives inner detector tracks reconstructed by IDSCAN in the region around the level-1 RoI and combine them with the track in the muon spectrometer. Both the muon spectrometer track and the inner detector tracks are extrapolated to a common surface on a cylinder of 425 cm radius around the beam axis that is outside the calorimeter but before the entrance to the muon system. A simple extrapolation method is used. It only takes into account the bending of the inner detector tracks in ϕ and the change of the direction in η for the muon spectrometer tracks. Inner detector track and muon spectrometer track η and ϕ coordinates on the surface are required to be within a matching window. For the track combination fullfilling this criterion a combined transverse momentum is calculated as an weighted average of $1/p_T$ of both tracks. Expected resolutions are taken as the weights. For muons with p_T below 50 GeV the muon spectrometer doesn't improve p_T resolution of the combined track but it only confirms that the inner detector track belongs to a muon. Selecting muon candidates for which an acceptable match is found between the muon spectrometer track and the inner detector track reduces the rate of muons from K and π decays-in-flight.

The performance of these algorithms was studied using Monte Carlo samples and it is presented in [8]. Apart from already mentioned algorithms there are other level-2 muon trigger algorithms that combine the information from the muon spectrometer with the one from the calorimeters to identify isolated muons. However, since b-physics triggers don't trigger on isolated muons we won't give any details on these algorithms.

3.5 Di-muon Triggers

A purpose of di-muon triggers is to trigger on processes that contain two muons in the final state. Since a total expected di-muon rate is approximately two orders of magnitude lower than the single muon one (see Figure 3.4), thresholds of the di-muon triggers can be lower than ones used for the single muon triggers.

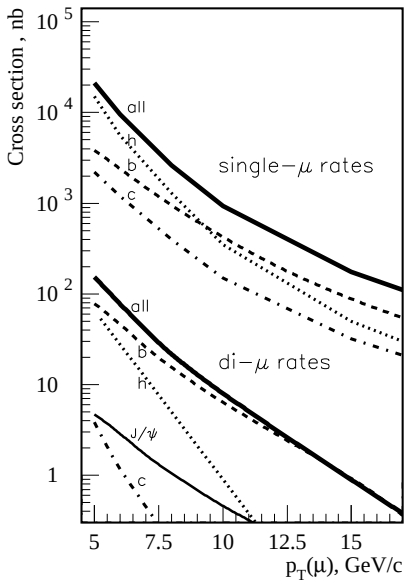

Figure 3.4: Single and di-muon cross sections [2].

There are two possible strategies how to trigger on di-muon processes. The first one requires the presence of two muons already at level-1. Both muon RoI's are then confirmed at level-2 using MuFast and MuComb algorithms. The second method starts from a single RoI that is confirmed at level-2 and identifies the second muon only at level-2 among tracks reconstructed in an extended region around the first muon. We will refer to triggers based on the first approach as *topological triggers* while the latter one as *single RoI triggers*. The difference is illustrated in Figure 3.5.

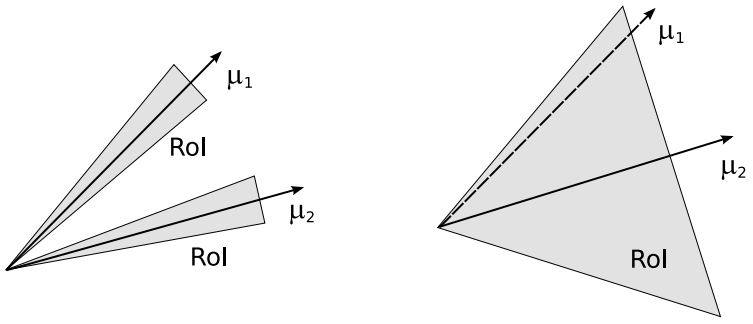

Figure 3.5: Schematic illustration of a di-muon reconstructed by the topological trigger (left) and the single RoI trigger (right). The dashed line in the right figure means that the second muon was reconstructed only at level-2.

Since both muons need to be reconstructed in one RoI, the single RoI triggers reconstruct larger region of the inner detector than the topological ones do. On the other hand their efficiency is usually higher since only one muon needs to have a high enough momentum to give rise to a level-1 RoI. Because of the higher level-1 rate, the single RoI triggers are expected to be used at the initial low luminosity run.

The core part of the single RoI trigger algorithms is implemented in the feature extraction algorithm *TrigDiMuon* [9]. It is a level-2 algorithm that starts from a level-1 RoI and reconstructs tracks in an extended region of the inner detector using IDSCAN (or SiTrack). In order to reduce an input rate it is possible to confirm the muon RoI by MuFast or MuComb first. The current default size of the region is $\Delta\eta \times \Delta\phi = 0.75 \times 0.75$. Since TrigDiMuon is designed to select primarily J/ψ particles and other resonances, the size of the region is chosen such that there is a probability of 92% to include the second J/ψ muon to the region [9]. This number was obtained when requiring p_{T} of the first muon to be greater than 6 GeV and the second one 3 GeV. If the thresholds are lowered to 4 GeV and 2.5 GeV the probability drops to 79%.

TrigDiMuon combines all the opposite charged tracks reconstructed in the region and if their invariant mass is greater than a certain threshold (2.8 GeV by default) it extrapolates them to the muon spectrometer to confirm whether they belong to muons. The extrapolation takes into account the bending of the trajectory in ϕ due to the solenoidal magnetic field and the bending in η due to the toroidal one. It is done using a formula that parametrises an expected bending. It takes into account inhomogeneity of the toroidal field in the end-cap by using a different parametrisation in each η and ϕ region. Track is considered as a muon candidate if there is a sufficient number of MDT hits in the road around the extrapolated track. The size of the road also differs for each η region.

Chapter 4

Semimuonic Rare Decays of B Hadrons

When talking about rare B decays one usually means Cabbibo-suppressed quark transitions $b \to u$ or transitions $b \to d$ and $b \to s$ that are forbidden at tree-level in the standard model. For that reason branching ratios of these processes are very low, i.e. in order of $10^{-5} - 10^{-6}$. In this chapter we present a very brief overview of the theoretical framework used for a description of decays with the latter two quark transitions. These involve *flavour changing neutral currents* (FCNC). In the standard model the lowest order contributions to these processes are represented by one-loop Feynman diagrams and they are a good testing ground for the standard model predictions. Also, because the tree-level contributions are forbidden, it would be possible to observe effects of non-standard model loop contributions which would be negligible in tree-level allowed processes. Thus these decays provide a way of searching for a new physics complementary to the direct searches. Apart from that, decay rates depend on the values $|V_{td}|$ or $|V_{ts}|$ of CKM matrix, thus the rate measurement complement their determination from $B^0 - \overline{B}^0$ mixing. More information on possible physics impacts of the B rare decays measurements at LHC can be found for instance in reference [16].

We distinguish three types of rare B decays: *purely leptonic*, *radiative* and *semileptonic*. The first case is represented for instance by the decay $B^0 \to \mu^+\mu^-$ where only muons are in the final state. Radiative decays have γ photon in the final state and are represented for instance by the decay $B^0 \to K^{*0}\gamma$. In this thesis we concentrate on the last type of the decays where leptons and hadrons can be found in the final state. Particularly, we study the cases where there are two opposite-charged muons in the final state. These cases are represented by the decays $B^+ \to K^+\mu^+\mu^-$, $B_d^0 \to K^{*0}\mu^+\mu^-$, $B_s^0 \to \phi^0\mu^+\mu^-$, $\Lambda_b \to \Lambda^0\mu^+\mu^-$, etc.

4.1 Theoretical Framework

The rare decays can be described by the following effective Hamiltonian [16]:

$$\mathcal{H}_{\mathrm{eff}}^{\mathrm{q}} = -\frac{4G_{\mathrm{F}}}{\sqrt{2}} V_{\mathrm{tb}} V_{\mathrm{tq}}^{*} \sum_{i=1}^{11} C_i(\mu) \mathcal{O}_i^{\mathrm{q}}(\mu), \tag{4.1}$$

where q is s or d-quark, G_{F} is Fermi constant, $V_{\mathrm{tb}}V_{\mathrm{tq}}^{*}$ are elements of CKM matrix, $C_i(\mu)$ are so called *Wilson coefficients* and $\mathcal{O}_i^{\mathrm{q}}(\mu)$ are local renormalised operators. The coefficients C_i can be calculated in some perturbation theory and they carry the information about a potentially new physics.

The Hamiltonian (4.1) was derived from the standard model, but it holds for a number of its extensions, for instance the minimal super-symmetric model (MSSM). However, the basis of operators $\mathcal{O}_i$ is not complete and in some theories (e.g. those exhibiting left-right asymmetries) the new physics can show up in a form of new operators.

The new physics will exhibit itself as so called *short distance* effects. It means that the differences from the standard model will show up at the level of interactions of individual quarks. However, quarks are confined in hadrons, hence the observed results will be strongly influenced by the *long-distance* effects at the hadronic scale. Because of these long-distance effects all the listed semimuonic decays will exhibit a different behaviour even though at the quark level they can all be represented by a single decay $\mathrm{b} \to \mathrm{s(d)}\,\mu^{+}\mu^{-}$.

For the semimuonic decays at the free-quark level the effective Hamiltonian (4.1) will look like [17]:

$$\begin{aligned}
\mathcal{H}(\mathrm{b} \to \mathrm{s}\,\mu^{+}\mu^{-}) \;=\; & \frac{G_{\mathrm{F}}\alpha}{\sqrt{2}\pi} V_{\mathrm{tb}} V_{\mathrm{ts}}^{*} \Big\{ \left[\bar{\mathrm{s}}\gamma_\alpha \left(C_9^{\mathrm{L}} P_{\mathrm{L}} + C_9^{\mathrm{R}} P_{\mathrm{R}}\right) \mathrm{b}\right] [\bar{\mu}\gamma^\alpha \mu] \\
& + \left[\bar{\mathrm{s}}\gamma_\alpha \left(C_{10}^{\mathrm{L}} P_{\mathrm{L}} + C_{10}^{\mathrm{R}} P_{\mathrm{R}}\right) \mathrm{b}\right] [\bar{\mu}\gamma^\alpha \gamma_5 \mu] \\
& - 2m_{\mathrm{b}} C_7^{\mathrm{eff}} \left[\bar{\mathrm{s}} i\sigma_{\alpha\nu} \frac{q^\nu}{s} \left(C_7^{\mathrm{L}} P_{\mathrm{L}} + C_7^{\mathrm{R}} P_{\mathrm{R}}\right) \mathrm{b}\right] [\bar{\mu}\gamma^\alpha \mu] \Big\},
\end{aligned} \tag{4.2}$$

where $s = q^2$, $q = p_+ + p_-$ is the sum of the muons momenta, $P_{\mathrm{L(R)}} = (1 \mp \gamma_5)$ and $C_i^{\mathrm{L(R)}}$ denote the Wilson coefficients for left- or right-handed couplings. The Hamiltonian leads to the free-quark decay amplitude:

$$\begin{aligned}
\mathcal{A}(\mathrm{b} \to \mathrm{s}\,\mu^{+}\mu^{-}) \;=\; & \frac{G_{\mathrm{F}}\alpha}{\sqrt{2}\pi} V_{\mathrm{tb}} V_{\mathrm{ts}}^{*} \Big\{ C_9^{\mathrm{eff}}(s) [\bar{\mathrm{s}}\gamma_\alpha P_{\mathrm{L}} \mathrm{b}] [\bar{\mu}\gamma^\alpha \mu] \\
& + C_{10} [\bar{\mathrm{s}}\gamma_\alpha P_{\mathrm{L}} \mathrm{b}] [\bar{\mu}\gamma^\alpha \gamma_5 \mu] \\
& - 2m_{\mathrm{b}} C_7^{\mathrm{eff}} \left[\bar{\mathrm{s}} i\sigma_{\alpha\nu} \frac{q^\nu}{s} P_{\mathrm{R}} \mathrm{b}\right] [\bar{\mu}\gamma^\alpha \mu] \Big\}.
\end{aligned} \tag{4.3}$$

Already this decay amplitude exhibits some long-distance effects caused by the $\bar{\mathrm{c}}\mathrm{c}$ resonances J/ψ, ψ' and ψ'' that will show up as peaks in the distribution of the

di-muon invariant mass. These effects are usually absorbed into the redefinition of the coefficient C_9 which becomes momentum-dependent [16].

To describe other long-distance effects we calculate matrix elements of the quark operators in (4.2) between the hadron states. It means we need the following expressions:

$$\langle h|\,\bar{\mathrm{s}}\gamma_\mu \mathrm{b}\,|h_\mathrm{b}\rangle, \langle h|\,\bar{\mathrm{s}}\gamma_\mu\gamma_5 \mathrm{b}\,|h_\mathrm{b}\rangle, \langle h|\,\bar{\mathrm{s}}i\sigma_{\mu\nu} \mathrm{b}\,|h_\mathrm{b}\rangle \text{ and } \langle h|\,\bar{\mathrm{s}}i\sigma_{\mu\nu}\gamma_5 \mathrm{b}\,|h_\mathrm{b}\rangle, \tag{4.4}$$

where h stands for the final state hadron and h_b stands for the mother B hadron. The expressions (4.4) are parametrised in terms of form factors. The parametrisation is different if h and h_b are mesons or baryons. Reference [16] uses the following form factors to parametrise the decay amplitude of $\mathrm{B}^0_\mathrm{d} \to \mathrm{K}^{*0}\mu^+\mu^-$:

$$\begin{aligned}
\langle \mathrm{K}^{*0}|\,\bar{\mathrm{s}}\gamma_\mu P_\mathrm{L} \mathrm{b}\,|\mathrm{B}^0_\mathrm{d}\rangle &= -i\epsilon^*_\mu(M+m)A_1(s) + i(p_\mathrm{B}+p)_\mu(\epsilon^* p_\mathrm{B})\frac{A_2(s)}{M+m} \\
&\quad + iq_\mu(\epsilon^* p_\mathrm{B})\frac{2m}{s}(A_3(s)-A_0(s)) + \epsilon_{\mu\nu\rho\sigma}\epsilon^{*\nu}p_\mathrm{B}^\rho p^\sigma \frac{2V(s)}{M+m}, \\
\langle \mathrm{K}^{*0}|\,\bar{\mathrm{s}}\sigma_{\mu\nu}q^\nu P_\mathrm{R} \mathrm{b}\,|\mathrm{B}^0_\mathrm{d}\rangle &= i\epsilon_{\mu\nu\rho\sigma}\epsilon^{*\nu}p_\mathrm{B}^\rho p^\sigma 2T_1(s) \\
&\quad + \left\{\epsilon^*_\mu(M^2-m^2) - (\epsilon^* p_\mathrm{B})(p_\mathrm{B}+p)_\mu\right\} T_2(s) \\
&\quad + (\epsilon^* p_\mathrm{B})\left\{q_\mu - \frac{s}{M^2-m^2}(p_\mathrm{B}+p)_\mu\right\} T_3(s)
\end{aligned} \tag{4.5}$$

with

$$A_3(s) = \frac{M+m}{2m}A_1(s) - \frac{M-m}{2m}A_2(s), A_0(0) = A_3(0) \text{ and } T_1(0) = T_2(0).$$

We designate ϵ the polarisation vector of K^{*0} meson, p_B and p momenta of B^0 and K^{*0} meson and M and m their masses. Form factors must be calculated in a theory, which is a non-trivial problem since they are essentially non-perturbative. See for instance [18] for details on a calculation of the form factors that was done using the *QCD sum rules on the light cone*. Here we won't go into details, let us just mention that the form factors can be parametrised as:

$$F(s) = F(0)\exp\left(c_1\frac{s}{M^2} + c_2\frac{s^2}{M^4}\right). \tag{4.6}$$

For the central values of the coefficients c_1 and c_2 we refer the readers again to [16]. We won't state explicit expressions for decay rates and spectra in terms of the matrix elements (4.5) but turn our attention to the quantity that is the most important for ATLAS rare decays measurements. It is *forward-backward* asymmetry A_FB which is defined as [16]:

$$A_\mathrm{FB}(s) = \frac{1}{d\Gamma/ds}\left\{\int_0^1 d\cos\theta \frac{d^2\Gamma}{ds\,d\cos\theta} - \int_{-1}^0 d\cos\theta \frac{d^2\Gamma}{ds\,d\cos\theta}\right\}, \tag{4.7}$$

where θ is an angle between the momenta of the B meson and the μ^+ in the di-lepton centre-of-mass system. The asymmetry is governed by

$$A_{\mathrm{FB}} \propto C_{10}\Big[\Re C_9^{\mathrm{eff}}(s)V(s)A_1(s) - \frac{m_{\mathrm{b}}M}{s}C_7^{\mathrm{eff}}\left\{V(s)T_2(s)\left(1-\frac{m}{M}\right)+A_1(s)T_1(s)\left(1+\frac{m}{M}\right)\right\}\Big] \quad (4.8)$$

and in the standard model it will have a zero if $s = s_0$ given by the equation

$$\Re C_9^{\mathrm{eff}}(s_0) = -\frac{m_{\mathrm{b}}M}{s_0}C_7^{\mathrm{eff}}\left\{\frac{T_2(s)}{A_1(s)}\left(1-\frac{m}{M}\right)+\frac{T_1(s)}{V(s)}\left(1+\frac{m}{M}\right)\right\}. \quad (4.9)$$

There is a theoretical reason coming from the *large energy effective theory* (LEET) to assume that in ratios of the form factors in Equation (4.9) all dependence on intrinsically non-perturbative quantities cancels. One then gets an extremely simple form of the equation [16]:

$$\Re C_9^{\mathrm{eff}}(s_0) = -2\frac{m_{\mathrm{b}}M}{s_0}\frac{1-s_0/M^2}{1-(m/M)^2-s_0/M^2}\,C_7^{\mathrm{eff}}. \quad (4.10)$$

Note that the forward-backward asymmetry vanishes only if the signs of the coefficients C_7^{eff} and $\Re C_9^{\mathrm{eff}}$ are opposite. The precision of the zero-point of the forward-backward asymmetry is determined essentially by the precision of the ratio of the effective coefficients and m_{b} and is largely independent on hadronic uncertainties.

Calculations made within the standard model predict $s_0 \approx 2.9\ \mathrm{GeV}^2$. On the other hand, some standard model extensions like several SUSY models predict that there is no zero below the mass of $\bar{\mathrm{c}}\mathrm{c}$ resonances. Therefore, Equation (4.10) provides a way how to distinguish between the standard model and some beyond-standard model scenarios. Figure 4.1 shows the forward-backward asymmetry for the standard model and two SUSY models.

Note that the analysis of $\mathrm{B}_{\mathrm{s}}^0 \to \phi^0\mu^+\mu^-$ parallels exactly that of $\mathrm{B}_{\mathrm{d}}^0 \to \mathrm{K}^{*0}\mu^+\mu^-$. However, the presented formulae and considerations can't be immediately applied for process $\mathrm{B}_{\mathrm{d}}^0 \to \rho^0\mu^+\mu^-$. It's because for this process we must include contributions of $\bar{\mathrm{s}}\mathrm{s}$ resonances to C_9^{eff} coefficient, which are Cabbibo-suppressed in $\mathrm{B}_{\mathrm{d}}^0 \to \mathrm{K}^{*0}\mu^+\mu^-$ and $\mathrm{B}_{\mathrm{s}}^0 \to \phi^0\mu^+\mu^-$ processes. Unfortunately the theory tools that allow one to treat $\bar{\mathrm{c}}\mathrm{c}$ resonance contributions to $\mathrm{B}_{\mathrm{d}}^0 \to \mathrm{K}^{*0}\mu^+\mu^-$ are not applicable anymore.

Also, the semileptonic processes with a pseudoscalar in the final state – e.g. $\mathrm{B}^0 \to \pi\mu^+\mu^-$, $\mathrm{B}^0 \to \mathrm{K}^0\mu^+\mu^-$ or $\mathrm{B}^+ \to \mathrm{K}^+\mu^+\mu^-$ – can be viable sources of information on the short-distance physics. Their experimental detection is, however, more complicated and only the process with the charged kaon in the final state is going to be measured in ATLAS.

For the baryonic decays, e.g. $\Lambda_{\mathrm{b}} \to \Lambda^0\mu^+\mu^-$ we get a different form of matrix elements of the effective Hamiltonian (4.2) since the involved particles are

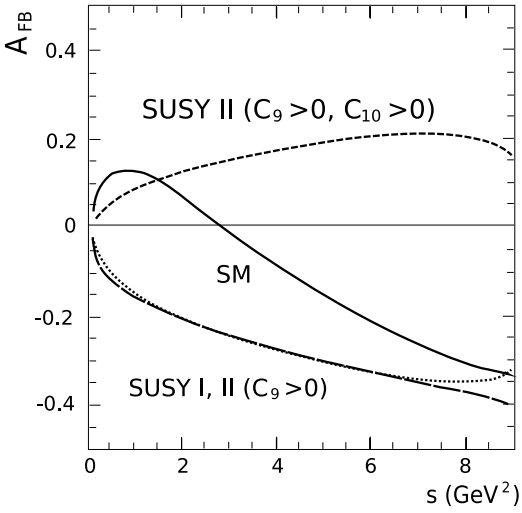

Figure 4.1: Forward-backward asymmetry of $B_d^0 \to K^{*0}\mu^+\mu^-$ in the standard model (solid line) and two SUSY models (dashed lines) [16].

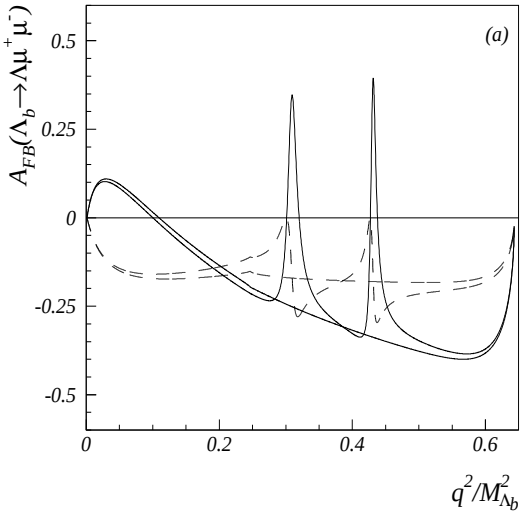

Figure 4.2: Forward-backward asymmetry of $\Lambda_b \to \Lambda^0\mu^+\mu^-$ in the standard model (solid line) and a generic SUSY model (dashed line). The curves with and without resonant shapes represent including and no long distance contributions [17].

fermions. The matrix elements are parametrised by the following form factors [17]:

$$\begin{aligned} H_1^\mu &= \bar{\Lambda}\gamma^\mu(A_1P_R + B_1P_L)\Lambda_b + \bar{\Lambda}\sigma^{\mu\nu}q_\nu(A_2P_R + B_2P_L)\Lambda_b, \\ H_2^\mu &= \bar{\Lambda}\gamma^\mu(D_1P_R + E_1P_L)\Lambda_b + \bar{\Lambda}\sigma^{\mu\nu}q_\nu(D_2P_R + E_2P_L)\Lambda_b \\ &\quad -q^\mu\bar{\Lambda}(D_3P_R + E_3P_L)\Lambda_b, \end{aligned} \tag{4.11}$$

and the decay amplitude can be written as:

$$\mathcal{A}(\Lambda_b \to \Lambda^0\mu^+\mu^-) = \frac{G_F\alpha}{\sqrt{2}\pi}V_{tb}V_{tq}^*\left\{H_1^\mu[\bar{\mu}\gamma_\mu\mu] + H_2^\mu[\bar{\mu}\gamma_\mu\gamma_5\mu]\right\}. \tag{4.12}$$

We note that the Wilson coefficients are contained in the form factors A_i, B_i, D_i and E_i. An explicit dependence on the coefficients can be seen in a different

parametrisation (for a definition of the new form factors see [17]):

$$\begin{aligned} A_i &= C_9^{\text{eff}} \frac{f_i - g_i}{2} - \frac{2m_\text{b}}{s} C_7^{\text{eff}} \frac{f_i^\text{T} - g_i^\text{T}}{2}, \\ B_i &= C_9^{\text{eff}} \frac{f_i + g_i}{2} - \frac{2m_\text{b}}{s} C_7^{\text{eff}} \frac{f_i^\text{T} - g_i^\text{T}}{2}, \\ D_i &= C_{10} \frac{f_i - g_i}{2}, \\ E_i &= C_{10} \frac{f_i + g_i}{2}. \end{aligned} \tag{4.13}$$

Calculations of the form factors were made within the *heavy quark effective theory* (HQET). The consequence of the calculations combined with the results of CLEO experiment [19] is that one can make a good approximation of the general form factors [17]:

$$\begin{gathered} \frac{f_2^\text{T} + g_2^\text{T}}{f_1 + g_1} \approx 1, \frac{f_1 - g_1}{f_2 - g_2} \approx \delta = 0, \frac{g_2}{f_2} \approx \frac{g_1^\text{T}}{f_1^\text{T}} \approx \frac{g_2^\text{T}}{f_2^\text{T}} \approx 1, \\ \frac{f_1^\text{T} + g_1^\text{T}}{f_1 + g_1} \frac{1}{s} \approx \frac{f_2 + g_2}{f_1 + g_1} \end{gathered} \tag{4.14}$$

and define new form factors

$$\bar{f} \equiv \frac{f_1 + g_1}{2} \text{ and } \rho \equiv M \frac{f_2 + g_2}{f_1 + g_1} = \frac{F_2}{F_1(s) + (m^2/M^2) F_1(s)}. \tag{4.15}$$

This time we denote M the mass of Λ_b baryon and m the mass of Λ^0. Authors of [17] use the QCD sum rules under the assumption of HQET to derive the form factors:

$$F_i(s) = \frac{F_i(0)}{1 + as + bs^2}, \tag{4.16}$$

for the values of the parameters see the cited reference.

Again, as in the case of the meson decays, we won't present an explicit formulation of the decay rate here, instead we refer the readers to the paper [17]. The forward-backward asymmetry of $\Lambda_\text{b} \to \Lambda^0 \mu^+ \mu^-$ can be expressed by the following formula [17]:

$$A_\text{FB}(s) = \frac{3}{2} \sqrt{\phi(s)} \sqrt{1 - \frac{m_\mu^2}{s}} \frac{R_\text{FB}(s)}{R_{\Lambda_\text{b}}(s)}, \tag{4.17}$$

where

$$\begin{aligned} R_\text{FB}(s) &= \frac{s}{M^2} \left[1 - 2\frac{m}{M}\rho - \left(1 - \frac{m^2}{M^2} \right) \rho^2 \right] \Re C_9^{\text{eff}} C_{10}^* \\ &\quad + 2\frac{m_\text{b}}{M} \left(1 - \frac{s}{M^2} \rho^2 \right) \Re C_7^{\text{eff}} C_{10}^* \text{ and} \\ \phi(s) &= \left(1 - \frac{m^2}{M^2} \right)^2 - 2\frac{s}{M^2} \left(1 + \frac{m^2}{M^2} \right) + \frac{s^2}{M^4}. \end{aligned} \tag{4.18}$$

An explicit form of R_{Λ_b} is rather complicated and can be found in [17]. We note that the main non-perturbative QCD effect from $\bar{f}$ has been factored out in Equation (4.17). Also, since ρ is a ratio of the form factors it is expected to be insensitive to the QCD models.

Similarly as for the meson case we can define the value of $s = s_0$ for which the asymmetry vanishes by the following equation:

$$\Re C_9^{\text{eff}}(s_0) = -\frac{2m_b M}{s_0}\frac{1-(s_0/M^2)\rho^2}{1-2(m/M)\rho-(1-m^2/M^2)\rho^2}\Re C_7^{\text{eff}}. \tag{4.19}$$

The calculation of ρ within HQET was made by the authors of [17] with the result $\rho \approx -0.26$. Note that in the equation (4.19) ρ stands either together with m/M or it is squared. Since both values are small we can simplify Equation (4.19) as:

$$\Re C_9^{\text{eff}}(s_0) = -\frac{2m_b M}{s_0}\frac{1}{1-2(m/M)\rho}\Re C_7^{\text{eff}}. \tag{4.20}$$

As in the case of $B_d^0 \to K^{*0}\mu^+\mu^-$ the value of s_0 is only sensitive to the Wilson coefficients. In the standard model the numerical value of $s_0 \approx 3.1$ GeV^2. As well as for the case of the meson decays, some beyond-standard model theories don't have a zero-point in the forward-backward asymmetry below the mass of $\bar{c}c$ resonances. The forward-backward asymmetry of $\Lambda_b \to \Lambda^0\mu^+\mu^-$ for the standard model and a generic SUSY model is shown in Figure 4.2.

4.2 Experimental Considerations

Strategies for an offline and online selection of the semimuonic rare B decays are described in papers [11, 14, 15]. ATLAS has a potential in studying the following decays:

- $B^+ \to K^+\mu^+\mu^-$,
- $B_s^0 \to \phi^0\mu^+\mu^-$, where ϕ^0 decays into K^+K^-,
- $B_d^0 \to K^{*0}\mu^+\mu^-$, where K^{*0} decays into $K^+\pi^-$,
- $\Lambda_b \to \Lambda^0\mu^+\mu^-$, where Λ^0 decays into $p\pi^-$ and
- $B^+ \to K^{*+}\mu^+\mu^-$, where K^{*+} decays into $K_S^0\pi^+$ and K_S^0 into pions.

The processes involving antiparticles are going to be studied, too. Authors of the paper [11] implemented the theoretical models describing each process into the Monte Carlo generator and calculated the theoretical shapes of the differential cross section and forward-backward asymmetry. The samples were reconstructed using the ATLAS reconstruction software [29].

The offline analysis consists of two steps. In the first one all the final state tracks are reconstructed by the offline tracking algorithms. Then these tracks are

used to identify the studied process and reject a combinatorial background. The key tool of the analysis is a *vertex fitting*. Vertex fitters are software tools that can find the closest approach of multiple tracks and using a maximum likelyhood fit adjust their parameters so the tracks actually intersect. The offline vertex fitters allow to fit complicated topologies of subsequent decays with a number of constraints on invariant masses and origin of the primary particle. Cuts on the parameters describing the decay were then used to select the signal process and reject the combinatorial background. The used parameters and cuts are described in details in reference [11].

Considering extremely low branching ratios of the studied decays it is clear that one must use a very strict selection since background processes have the cross sections higher of several orders of magnitude. Consequently, such a selection will also reject a large fraction of the signal events. The references [11, 14, 15] estimate the efficiency of the offline selection to be in order of few %. This means that the uncertainty of the results will be dominated by the statistical error. However, one must also investigate an influence of systematics in order to be able to correctly interpret the results.

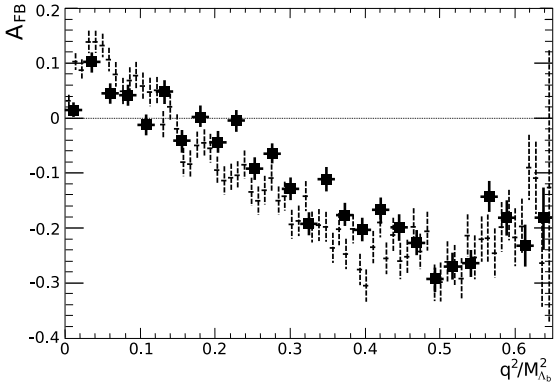

Figure 4.3: Impact of the explicit p_{T} cuts on the forward-backward asymmetry. The crosses shows the theoretical prediction without cuts while squares shows the asymmetry after one muon was required to have $p_{\mathrm{T}} > 6$ GeV and the other $p_{\mathrm{T}} > 4$ GeV. The figure was taken from [26].

In the measurement, the forward-backward asymmetry (defined by Formula (4.7)) is going to be estimated by the ratio:

$$A_{\mathrm{FB}} = \frac{N_{\mathrm{F}} - N_{\mathrm{A}}}{N_{\mathrm{F}} + N_{\mathrm{A}}}, \tag{4.21}$$

where N_{F} is the number of events with $\cos\theta^* > 0$ and N_{B} is the number of events with $\cos\theta^* < 0$. The great advantage of this quantity is that in the ratio a lot of systematic uncertainties cancels. Even though this is true for most of the systematics, there are some influences that change the shape of $\cos\theta^*$ distribution

and thus can change the value of the asymmetry. Since this thesis is devoted mainly to the trigger selection, we will comment on the influence of the explicit cuts on the final state muon momenta.

Figure 4.3 shows the standard model prediction of the forward-backward asymmetry for $\Lambda_b \to \Lambda^0 \mu^+ \mu^-$ as a function of q^2 (crosses) and how does it change when the muons are required to have $p_T > 6(4)$ GeV (squares). Note that an absolute value of the asymmetry is lower for the case with the cuts. It's because there is a correlation between the muons momenta and the decay angle $\cos\theta^*$. If we imply the cuts on p_T we restrict the kinematically allowed values of $\cos\theta^*$ which consequently change the asymmetry. However, this effect is well understood and can by easily included into the theoretical prediction.

An example of the results of the offline analysis of $\Lambda_b \to \Lambda^0 \mu^+ \mu^-$ is shown in Figures 4.4 and 4.5 (taken from [26]). In the left plot there is a spectrum of q^2 of the generated sample and the sample after the offline selection. The right plot shows the forward-backward asymmetry. Because of the limited statistics, the values are evaluated only in three points, taking the average of the asymmetry in three intervals of q^2. The errorbars were scaled to correspond to the yield at an integrated luminosity of 30 fb^{-1}. For this integrated luminosity an expected number of reconstructed and identified events is about 1500 events [14, 26], which allows to distinguish at a confidence level of 1.6σ the standard model prediction and the prediction of models having A_{FB} different by more than 8%.

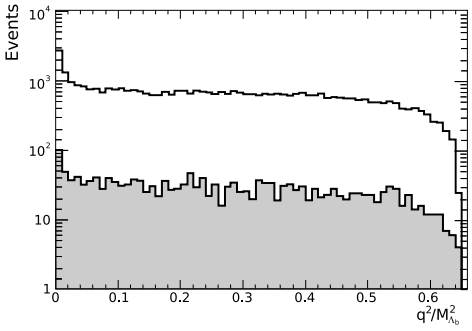

Figure 4.4: Di-muon invariant mass spectrum of $\Lambda_b \to \Lambda^0 \mu^+ \mu^-$. The open histogram shows the standard model-predicted spectrum and the filled histogram shows the spectrum after the offline reconstruction [26]. The theoretical model doesn't take into account the effect of $\bar{c}c$ resonances.

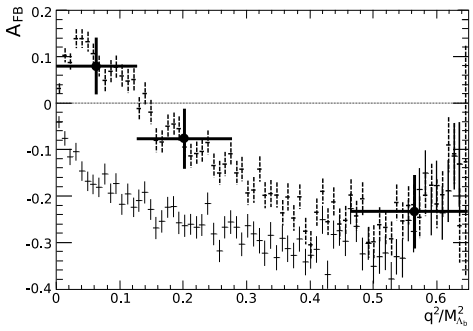

Figure 4.5: Forward-backward asymmetry of $\Lambda_b \to \Lambda^0 \mu^+ \mu^-$. Dashed crosses correspond to the asymmetry predicted by the standard model while solid crosses correspond to the asymmetry predicted by the model with the positive C_7^{eff} [26]. Experimental points are indicated by circles with large error bars.

Chapter 5

Monte Carlo Data Samples

For performance studies presented in this thesis *Monte Carlo samples* were used. Monte Carlo samples are data samples that looks moreless the same as the real data samples, but all the physics processes have been simulated using Monte Carlo generators. Also, the simulation of the ATLAS detector has been used to mimic its response.

The samples are created in the following steps:

Generation: physics processes that occur at proton-proton collisions are simulated using Monte Carlo generators. Our samples were created using the generators called *Pythia B* and *EvtGen* [12, 20]. Unstable particles are decayed and the output of the simulation are momenta and directions of the stable particles. In order to save computing resources, some pre-selection is usually being applied on particles that are likely to be rejected by the trigger. For that reason di-muon samples are often produces with the requirement that one muon has $p_{\mathrm{T}} > 4$ GeV and the other 6 GeV.

Propagation: simulation of the particle propagation through the detector using the tool called *Geant 4* [22]. Geant calculates the trajectories of the particles through the matter taking into account the effects such as energy loss and multiple scattering in a detector material as well as a production of secondary particles (δ-electrons, showers, etc.). Output of this simulation is an energy deposited in an active volume in each ATLAS subdetector.

Digitisation: simulation of the ATLAS detector. The information on the deposited energy is translated into the detector response, i.e. information that will be read out and stored on tapes (raw data). Output from this step is already looking like the real data samples. The only difference is that there is an information about the physics process – so called *Monte Carlo truth* information – stored along with the detector output. This truth information is essential for performance studies since one needs to know the topology of the generated process in order to see whether his analysis identified it correctly.

Reconstruction: reconstruction of the raw data using actual ATLAS reconstruction software [29]. This step will already be the same for the real data. The difference is that real data will be available only after a trigger selection while in the case of Monte Carlo samples the trigger algorithms are usually run parallel to the offline reconstruction and the information on a trigger decision is saved in the output sample without actually excluding the events that haven't passed the trigger selection. The output of the reconstruction are identified physics objects e.g. electron, τ-lepton and muon tracks, jets, missing transverse energy, etc.

Physics analysis: analysis of the reconstructed samples in order to identify studied processes and to extract relevant physics quantities.

Process	Format	Generator pre-select.	Cross section	No. of events
$\Lambda_b \rightarrow \Lambda^0 \mu^+ \mu^-$	Raw	$p_T(\mu_{1(2)}) > 6\,(4)$ GeV	1.2 pb	1200
$\Lambda_b \rightarrow \Lambda^0 \mu^+ \mu^-$	Recon.	$p_T(\mu_{1(2)}) > 6\,(4)$ GeV	1.2 pb	50000
$bb \rightarrow \mu^+ \mu^- X$	Raw	$p_T(\mu_{1(2)}) > 6\,(4)$ GeV	110.5 nb	1200
$bb \rightarrow J/\psi(\mu^+ \mu^-)X$	Recon.	$p_T(\mu_{1(2)}) > 6\,(4)$ GeV	11.06 nb	80000
$pp \rightarrow J/\psi(\mu^+ \mu^-)X$	Recon.	$p_T(\mu_{1(2)}) > 6\,(4)$ GeV	21.75 nb	75250

Table 5.1: Data samples used for the performance studies. The cross sections were taken from [13] and [11].

In this thesis we use fully reconstructed samples for the calibration studies as well as samples after digitisation for development and performance study of the rare B decay algorithm. The used samples are listed in Table 5.1.

Chapter 6

Trigger Selection of Semimuonic Rare Decays

The list of the semimuonic rare B decay channels that are planned to be measured at ATLAS is shown in Chapter 4.2. We would like to have a common trigger algorithm that is able to select all the channels with an efficiency as high as possible. All final states of the listed processes contain a di-muon $\mu^+\mu^-$ together with some other particles. It means, that the invariant mass of the di-muon doesn't form a peak and can't be used as a primary selection criterion. However, the presence of the di-muon is essential for the background rate suppression (see Figure 3.4).

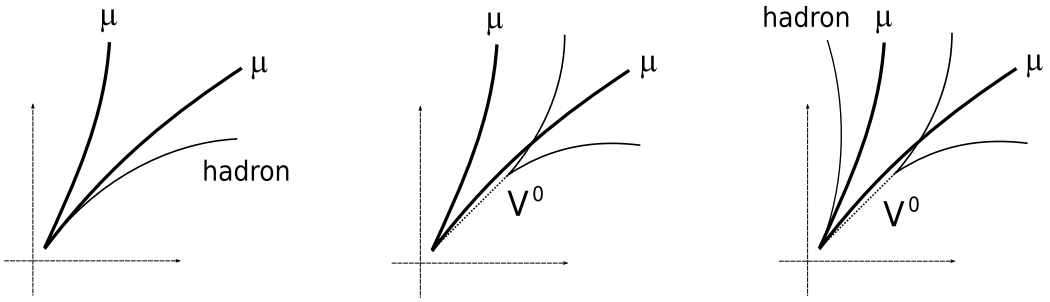

Figure 6.1: Topologies of semimuonic rare decays. The first toplogy is represented by decays where all the charged final state hadrons are coming from the vertex common with the di-muon (left). In the second topology, the charged-hadron tracks are decay product of a long-living neutral particle V^0 (middle). The last topology is a combination of the previous two (right).

The decays form three topologies according to the hadronic part of the final state. A schematic picture of these topologies is shown in Figure 6.1. The first topology is represented by the first B^+ decay, B_s^0 and B_d^0 decays and it is shown at the left side of the figure. Here one or two hadron tracks are coming from the vertex common with the muon tracks. In the second topology – represented by

Λ_b decay – hadron tracks form Λ^0 particle that originated in the muon tracks vertex but decayed far from it. In the figure, this topology is shown in the middle. Finally, the last topology is the combination of the previous two and it is represented by the second B^+ decay. It is shown at the right side of the figure.

There are two basic strategies how to trigger on these processes. They differ in a way how they reconstruct the final state muons. The first method starts from a single level-1 muon RoI and reconstructs the di-muon using TrigDiMuon algorithm (single RoI trigger). The second method requires a presence of two muon RoI's already at level-1, which are then confirmed at level-2 (topological trigger). A schematic diagram showing the sequence of algorithms used by those two triggers is shown in Figure 6.2.

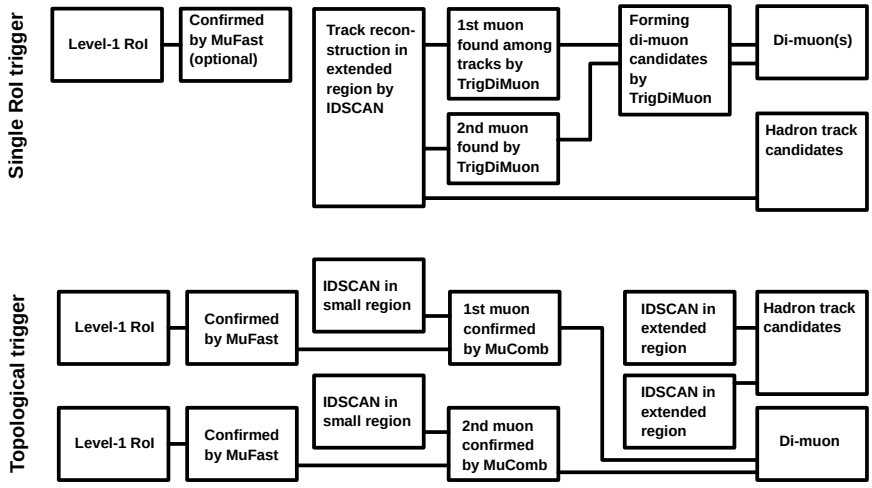

Figure 6.2: Di-muon part of the trigger algorithm.

Hadronic part of the final state is reconstructed at level-2. In the single RoI triggers the hadron tracks are reconstructed together with the second muon in the extended inner detector region. In topological triggers the tracks must be reconstructed in the extended regions around both RoI's after they are confirmed by level-2. The size of the regions is determined from the topology of the event. It means that the size should be such that the substantial part of the hadron tracks lies within the region. On the other hand, one should try to keep these regions as small as possible because the tracking is time consuming.

When the tracks are reconstructed they are passed to the algorithm which reconstructs and identifies the physics processes (*b-physics hypothesis algorithm*). The algorithm can use the following selection criteria: firstly, it can cut on track parameters like charge or transverse impact parameter a_0 to reduce number of candidate tracks. Secondly, it can combine multiple tracks and cut on their invariant mass. This is an efficient way how to select decay products of some unstable particle. The most sophisticated way of a selection is the vertex fitting. This way

one can identify the tracks coming from a single point in space and significantly reduce the combinatorial background. Also, the invariant mass calculated by the fitter is more accurate since the fitter uses the refined track parameters evaluated in the vertex (note that track parameters of a single track are always taken at the perigee of the track). Cuts on the quality of the vertex fit (χ^2) and the mass calculated in the vertex can be applied after the vertexing. The down side of the vertex fitting is that it is time consuming.

Before we start to investigate possible selection algorithms let us define several basic concepts that we will need later. First of all, an efficiency of a trigger selection can be estimated as follows:

$$\epsilon = \frac{N_{\text{trig}}}{N}, \tag{6.1}$$

where N is the number of the events containing our signal process and N_{trig} is the number of those events that were accepted by the trigger. Apart from the signal events the trigger will also accept some events containing the processes that we are not interested in or so called *background*. To describe amount of background events rejected by the trigger we use the quantity called *trigger rejection factor*

$$r = 1 - \epsilon_{\text{back}}, \tag{6.2}$$

where ϵ_{back} is the trigger efficiency for the background events. The goal of every trigger algorithm developper is to achieve the highest possible efficiency together with the highest background rejection.

6.1 Trigger Algorithm with the Full Λ^0 Reconstruction

We propose the following procedure for the selection of the semimuonic rare decays:

1. Level-1 trigger. One or two muon RoI's above certain p_{T} threshold are required by the single RoI trigger or the topological trigger respectively.

2. Level-2 muon trigger. The muon RoI's are confirmed by the level-2 muon reconstruction algorithms (MuFast and then MuComb).

3. Tracks are reconstructed in the extended regions around the level-1 RoI's (see Figure 6.2). In the case of the single RoI trigger the second muon track is identified among these tracks using the extrapolation to the muon system. The available inner detector tracking algorithms are IDSCAN and SiTrack, but in this thesis all the studies were made using IDSCAN.

4. Cut on the invariant mass of the di-muons. The invariant mass can have the following values $2m_\mu \leq M_{\mu\mu} \leq (M - m)$ where M stands for the mass

of the mother particle and m for the mass of the final state hadron. Since the muon mass m_μ is small compared to the mass of b-hadrons we use only the higher cut. The schematic diagram of the b-physics hypothesis part of the algorithm is shown in Figure 6.3.

5. Selection of the hadron tracks candidates. There are the following possible combinations of the final state hadron tracks: one positive track ($B^+ \to K^+\mu^+\mu^-$), two opposite-charged tracks ($B_s^0 \to \phi^0\mu^+\mu^-$, $B_d^0 \to K^{*0}\mu^+\mu^-$ and $\Lambda_b \to \Lambda^0\mu^+\mu^-$) and finally two positive tracks and one negative ($B^+ \to K^{*+}\mu^+\mu^-$). If the event doesn't contain any of these combinations it can be rejected straight away. In order to save the computing resources and time it is reasonable to create one collection of all positive tracks and one collection of opposite-charged track combinations. The three-tracks combinations should be created later – after a cut on the invariant mass of K^0 is applied on the track pairs.

6. There is a possibility to apply cuts on the transverse impact parameter a_0 of the decay products of V^0's (i.e. K^0 and Λ^0). Because the significant fraction of V^0's decays far from the point of their origin, the distribution of the impact parameter of their decay products is broader than the one of the tracks originated in the point of proton-proton collisions. This cut could provide a way how to reduce the number of candidate tracks, however the performance study presented in Chapter 6.3.1 shows that it unacceptably lowers the efficiency. If we decide to use these cuts, we must keep the collection of Λ^0 and K^0 final state candidates separately from the other opposite-charged tracks where no a_0 cuts were applied.

7. Di-muon vertexing. The tracks of the final state muons should intersect in the single point in space since they come from the same particle. Therefore, the vertexing is a good way how to reduce the contribution of the background processes, e.g. $b\bar{b} \to \mu\mu$. The cut on the vertex fit quality can be applied.

8. Cuts on invariant masses. The collection of the positive tracks is combined with the di-muon and the cut on the invariant mass of B^+ is applied. The invariant mass of each opposite-charged track pair from the collection is calculated and if it satisfies Λ^0, ϕ^0 or K^{*0} mass hypothesis it is combined with the di-muon and the cut on the invariant mass of Λ_b, B_s^0, respectively B_d^0 is applied. Finally, if the invariant mass of the pair satisfies K^0 mass hypothesis the pair is combined with the positive tracks and the di-muon and the cut on invariant mass of B^+ is applied. If none of the mass hypotheses is satisfied the event can be rejected.

9. Vertexing. From the point 8 the list of the final state track candidates for all the processes is available. For $B^+ \to K^+\mu^+\mu^-$, $B_s^0 \to \phi^0\mu^+\mu^-$ and $B_d^0 \to$

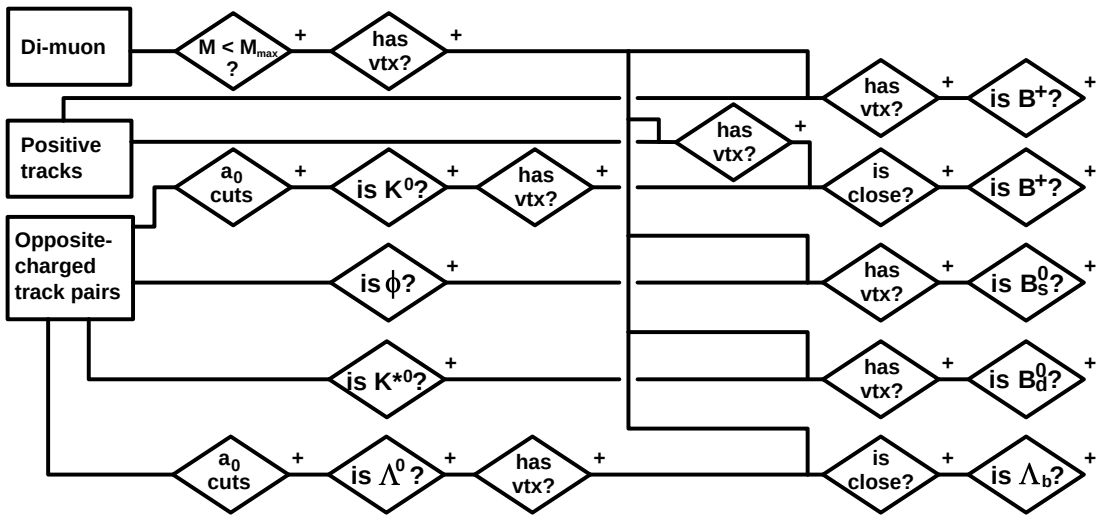

Figure 6.3: B-physics hypothesis part of the trigger algorithm. Diamonds represent the selection cuts applied on candidate track combinations. If the selection criterion is not fullfiled, the combination is rejected. Otherwise, it is passed to the next selection. Plus signs indicate the positive outcome of the selection.

$K^{*0}\mu^+\mu^-$ processes all the final state tracks should originate in the same vertex, hence three separate vertex fits can be performed for each collection of the final state candidates. The level-2 vertex fitter (TrigL2VtxFitter) allows to set mass constraints on the pairs of hadron tracks which can be exploited in the case of $B_s^0 \to \phi^0\mu^+\mu^-$ and $B_d^0 \to K^{*0}\mu^+\mu^-$ where the hadron tracks satisfy ϕ^0 or K^{*0} mass hypothesis. For the processes $\Lambda_b \to \Lambda^0\mu^+\mu^-$ and $B^+ \to K^{*+}\mu^+\mu^-$ the vertex fit can be used to reconstruct Λ^0 and K^0. In the case of $B^+ \to K^{*+}\mu^+\mu^-$ we can in addition require a common vertex of the pion from K^{*+} decay and the muons. The algorithm should allow us to switch on and off each of these vertexings. Appropriate mass and χ^2 cuts as well as the necessity of the vertexing must be determined from a detailed performance study.

10. V^0 distance. The last step that is remaining is to check whether Λ^0 and K^0 originated in Λ_b and K^{*+}, respectively. This can be done only in the case that V^0 and the di-muon vertices were reconstructed. The trigger level-2 vertex fitter doesn't allow to fit the tracks of neutral particles. However, from V^0 vertex we can obtain a direction of the mother particle momentum. The calculation of the distance between V^0 particle track and the vertex of

the di-muon is then straightforward:

$$\vec{s} = -\left[(\vec{r}_{\mathrm{V}^0} - \vec{r}_{\mu\mu}) \cdot \frac{\vec{p}_{\mathrm{V}^0}}{|\vec{p}_{\mathrm{V}^0}|}\right] \frac{\vec{p}_{\mathrm{V}^0}}{|\vec{p}_{\mathrm{V}^0}|},$$
$$d = |\vec{s} + \vec{r}_{\mathrm{V}^0} - \vec{r}_{\mu\mu}|, \tag{6.3}$$

where $\vec{r}_{\mathrm{V}^0}$ and $\vec{r}_{\mu\mu}$ are the positions of the vertices of V^0 particle and the di-muon respectively. $\vec{p}_{\mathrm{V}^0}$ is the vector of V^0 momentum. A cut on the distance d can be applied.

6.2 Trigger Algorithm with the Partial Λ^0 Reconstruction

As the performance study presented in Chapter 6.3.1 indicates, the trigger reconstruction efficiency of Λ^0 won't be very high. We suggest an alternative method of triggering on Λ_b decay. It profits from the fact that Λ^0 decays into two unequally massive particles – proton and pion. Since proton is almost seven-times heavier than pion it will carry a larger fraction of Λ^0 momentum and its direction will be similar to the original one. Therefore we can reconstruct an approximate mass (or *pseudo-mass*) of Λ_b by combining the proton track with the di-muon and substituting the proton mass by Λ^0 one. The pseudo-mass peak will be broader than the one from the full reconstruction, thus this algorithm will accept more background events. On the other hand, this way we can recover a substantial part of the events where the pion wasn't reconstructed.

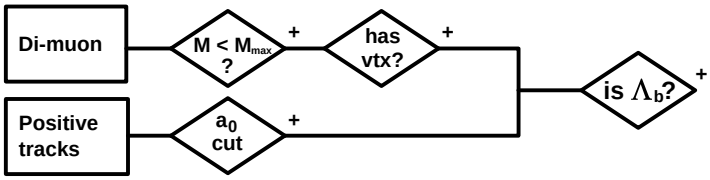

Figure 6.4: Partial Λ^0 reconstruction.

Λ_b part of the algorithm is shown in Figure 6.4. It combines positive tracks with the di-muon and apply the invariant mass cut. No vertex fit can be used on these three tracks since they are not coming from a single point. However, the vertexing on the muon tracks can be still performed. The rest of the algorithm for triggering the other decays remains the same.

Unfortunately this method can't be probably used for the K^0 reconstruction since it decays into pions so the momentum will be hand out more equally. For this channel the full reconstruction must be used.

6.3 Performance Study

In this chapter we study a performance of the topological trigger variant of the proposed algorithm using Monte Carlo samples of the process $\Lambda_b \to \Lambda^0(p\pi)\mu^+\mu^-$ (see Chapter 5). Since we study the performance on this single process the algorithm was simplified and it keeps only one collection of the opposite-charged track combinations that are considered to be candidates of Λ^0 decay products. The trigger performance for some other processes is studied in [11].

The algorithm code is available in author's space at CERN CVS server.

6.3.1 Topological Trigger for $\Lambda_b \to \Lambda^0(p\pi)\mu^+\mu^-$

The first step of every trigger performance study is the identification of the studied process in Monte Carlo truth information stored in the data samples. At the design-time of trigger algorithms it is essential to have the information about the simulated processes to see whether our reconstruction was successful and to determine its efficiency.

Once our process was found in the Monte Carlo truth information, distributions of a true transverse momentum p_T and a pseudorapidity η of the final state muons, the pion and the proton were made. They are shown in the figures in Appendix A. The two peaks at 4 GeV and 6 GeV in p_T distribution of the muons are the result of kinematic cuts made at the generater level of the simulation where one muon was required to have $p_T > 4$ GeV and the other 6 GeV. These pre-selection criteria were imposed to save computing resources, since a large fraction of muons with p_T below these thresholds won't be reconstructed anyway due to the trigger selection. Note that while the muons and proton p_T spectra are quite broad the distribution of the pion p_T is narrow and most of the particles have p_T below 3 GeV.

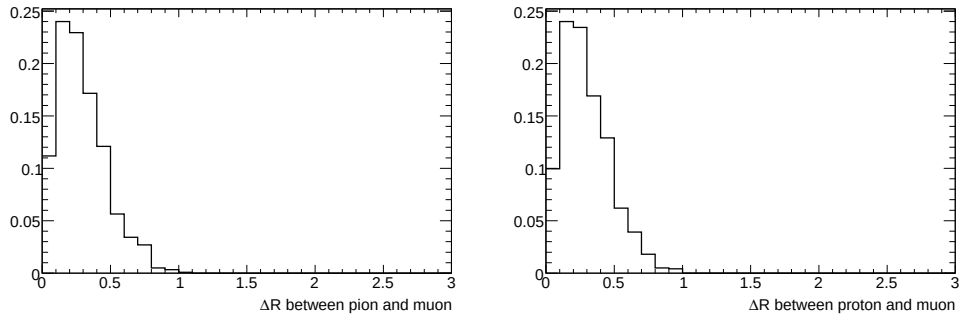

Figure 6.5: Distribution of the distance between the pion (left) and the proton (right) and the closer of the muons.

Figure 6.5 shows the distance $\Delta R = \sqrt{\Delta\eta^2 + \Delta\phi^2}$ of the pion or proton to the closer of the muons. This distribution is important in order to determine

an optimal size of the inner detector region where the tracks are reconstructed. Two settings were used in this performance study: one with the inner detector reconstruction window with size $\Delta\eta \times \Delta\phi = 1.5 \times 1.5$ and the other with $\Delta\eta \times \Delta\phi = 3 \times 3$. While the second window size is large enough to recover all the proton and pion tracks, the first one cuts off a small fraction of the tracks. However, since it is the standard window size of the b-physics level-2 reconstruction algorithm (called *IDSCAN_Bphysics*) we would like to use this setting.

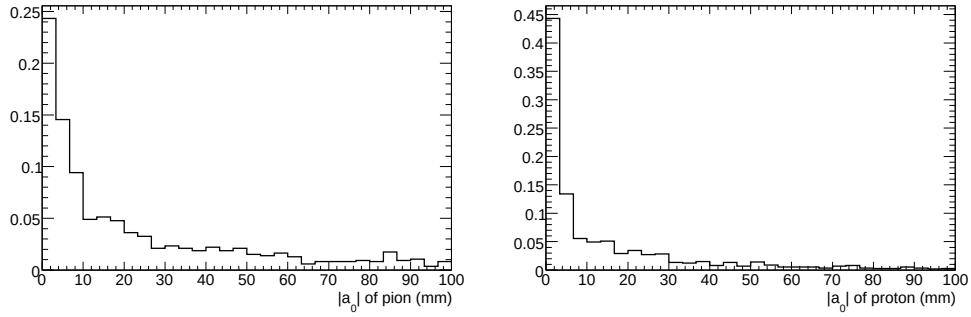

Figure 6.6: Distribution of the true transverse impact parameter a_0 of the pion (left) and the proton (right).

Another important distribution is the one of the proton and pion track transverse impact parameter a_0. It is shown in Figure 6.6. In order to reduce the number of tracks, the level-2 track reconstruction algorithm IDSCAN introduce an explicit cut on the impact parameter. Standard value of this cut for b-physics setting of the algorithm is $a_0 \leq 4$ mm. From Figure 6.6 it is evident that such a tight cut rejects a large fraction of the final state protons and the substantial one of the pions. For the purpose of this study we have loosened the cut to 50 mm, but we have investigated the performance with the standard b-physics setting, too. Together with the different reconstruction window sizes it gives four possible settings, however, we have studied only three of them. The settings of the parameters are summarised in Table 6.1.

Setting no.	Description	Window size $\Delta\eta \times \Delta\phi$	a_0 cut
1	Standard IDSCAN_Bphysics	1.5×1.5	4 mm
2	Large a_0 cut	1.5×1.5	50 mm
3	Large window and a_0 cut	3×3	50 mm

Table 6.1: Used settings of the level-2 track reconstruction algorithm IDSCAN.

The samples were reconstructed by the ATLAS trigger software [29] (the software simulation of level-1 trigger was used since the real one is hardware based

and can't work on Monte Carlo samples). For the purpose of performance studies this software provides information about a *hit-based matching* between true particles and reconstructed tracks. It means that each reconstructed track contains information about number of space points that lies on the track and have been caused by the true particle. This way we can determine, whether tracks of the final state particles have been reconstructed and calculate a reconstruction efficiency. It can be estimated as a ratio of number of true particles with reconstructed tracks N_{trig} to the total number of true particles N, all as a function of some kinematic variable.

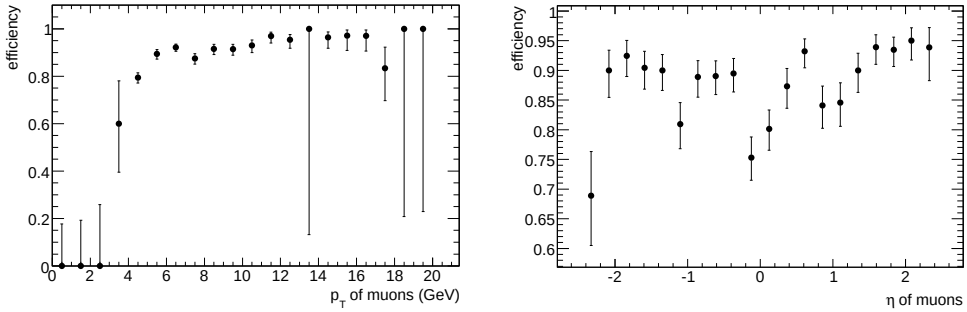

Figure 6.7: Level-2 reconstruction efficiency of the final state muons. An explicit cut $p_{\mathrm{T}} > 3$ GeV was applied on the reconstructed tracks. The efficiencies are expressed with respect to the number of the true muons.

Figure 6.7 shows the level-2 reconstruction efficiency of the final state muons as a function of p_{T} and η. The overall efficiency is quite high (around 90%) but it is a consequence of the kinematic pre-selection at the generator level. In reality a large fraction of the low p_{T} muon rate will be cut off by the trigger. Because the muon reconstruction precedes the run of IDSCAN in the b-physics setting, the muon efficiencies don't depend on IDSCAN reconstruction window size and the impact parameter cut. Therefore we show only one set of the plots for the muons. On the other hand, the reconstruction of the hadronic part of the final state strongly depends on the chosen IDSCAN setting. The reconstruction efficiency of the final state pion and proton as a function of p_{T} and a_0 are shown in Figure 6.8 (for setting no. 2) and in Appendix A (for all the settings).

An extremely low reconstruction efficiency of the final state pion indicates that the trigger with the full Λ^0 reconstruction won't be efficient for Λ_{b} events. The total efficiency of the the full final state reconstruction with respect to the events accepted by the di-muon trigger *mu6mu6* is 12% for the IDSCAN setting no. 1, 16% for the setting no. 2 and 17% for the setting no. 3. The efficiency w.r.t *mu6mu6* means that the number of all the signal events that passed the level-2 di-muon trigger designed to efficiently select muons with $p_{\mathrm{T}} \geq 6$ GeV was taken as a denominator in Formula (6.1) while the number of the events with the fully reconstructed Λ^0 final state was taken as a numerator. On the other hand, the

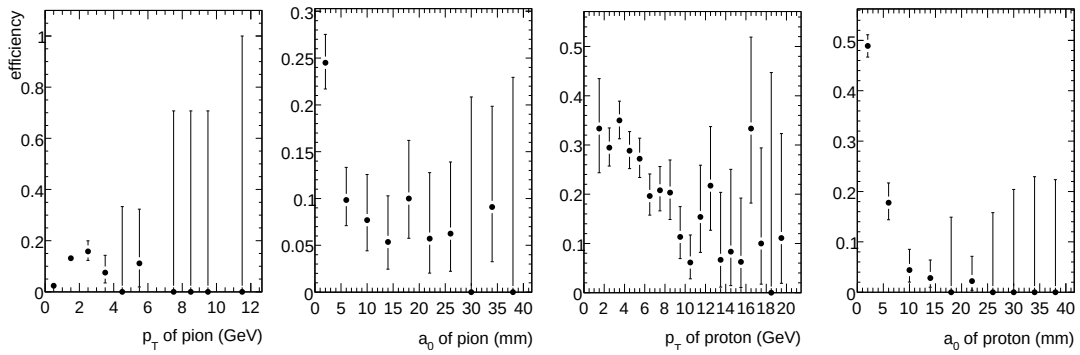

Figure 6.8: Level-2 reconstruction efficiency of the final state pion (two left plots) and proton (two right plots) of IDSCAN with the standard b-physics window size and loose a_0 cut (setting no. 2). The efficiencies are expressed with respect to the Monte Carlo truth.

total efficiency of the proton reconstruction with respect to the level-2 di-muon trigger *mu6mu6* is 66% for the setting no. 1 and 75% for the settings no. 2 and 3.

In order to estimate good selection cuts, we have constructed distributions of cut variables using the true-matching tracks. The following variables were used:

- di-muon invariant mass ($M_{\mu^+\mu^-}$),
- quality of the di-muon vertex fit (χ^2),
- impact parameters of the pion and proton (a_0),
- invariant mass of Λ^0 before the vertexing ($M_{\mathrm{p}\pi}$),
- quality of Λ^0 vertex fit (χ^2),
- invariant mass of Λ^0 after the vertexing (M_Λ),
- invariant mass of Λ_b ($M_{\mu^+\mu^-\mathrm{p}\pi}$),
- distance of Λ^0 track from the di-muon vertex and
- pseudo-mass of the partially reconstructed Λ_b for the trigger with the partial Λ^0 reconstruction.

Distributions of all the variables are shown in Appendix A. Here we show only the distribution of Λ^0 mass before and after the vertexing and the invariant mass of Λ_b (see Figure 6.9). Using the true-matching tracks the central values of the mass and the mass resolutions σ were calculated.

Cuts on Λ^0 and Λ_b mass were set to 3σ range around the central values. Cuts on the other variables were set open in order to get as high efficiency as

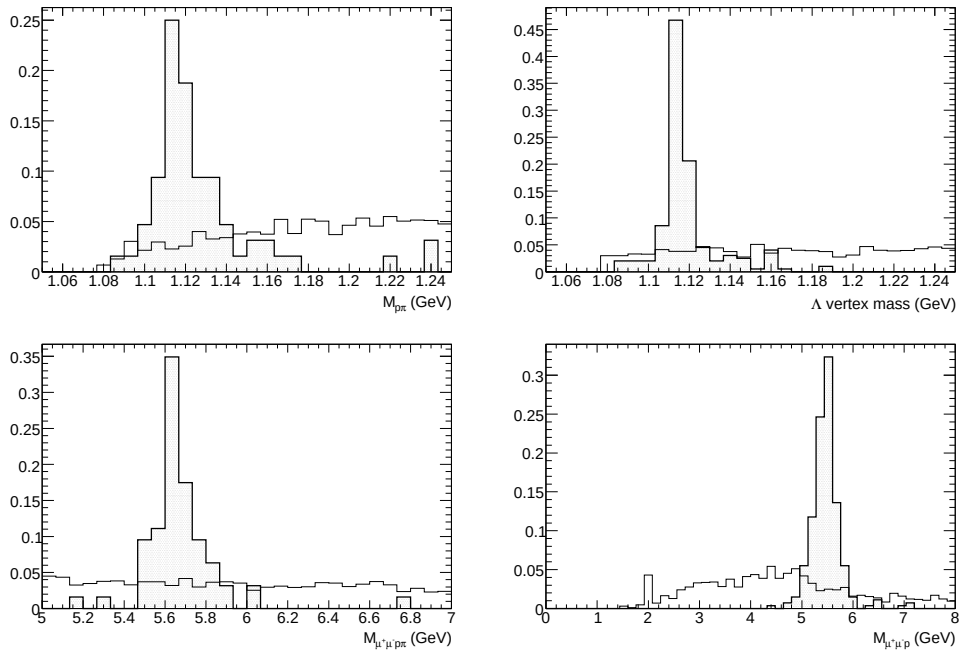

Figure 6.9: Distribution of Λ^0 mass before the vertexing (top left), Λ^0 mass after the vertexing (top right), the invariant mass of fully reconstructed Λ_b (bottom left) and the partially reconstructed Λ_b (bottom right). The shaded histograms were made using the true-matching tracks while the open ones were made using the background sample $b\bar{b} \rightarrow \mu^+\mu^-X$

possible. The cut on Λ^0 mass before the vertexing was set to 1.04 GeV $< M_{p\pi} <$ 1.22 GeV, the cut on Λ^0 mass after the vertexing was set to 1.07 GeV $< M_\Lambda <$ 1.16 GeV and the cut on Λ_b mass was set to 5.09 GeV $< M_{p\pi\mu^+\mu^-} <$ 6.27 GeV. The cut on invariant mass of the di-muon was set to $M_{\mu^+\mu^-} <$ 5 GeV. The trigger efficiencies were calculated with respect to the level-2 di-muon trigger *mu6mu6*. The efficiencies for different settings are shown in Table 6.2 together with background rejection factors. The background rejection was estimated using the sample $b\bar{b} \rightarrow \mu^+\mu^-X$ (see Chapter 5).

The performance of the trigger algorithm with IDSCAN setting no. 2 is basically the same as the one with the setting no. 3. It means that there is no need to extend the inner detector reconstruction window above the standard b-physics setting. On the other hand, the efficiency of the trigger with the loose IDSCAN impact parameter cut is about 30% higher than the one of the trigger with the tight cut. Despite this fact, when looking at the numbers in the table, one can only conclude that the efficiency of the trigger with the full Λ^0 reconstruction is low. A simple analysis made in Chapter 6.3.2 shows that we can improve the results by loosening the cuts. However, we should be carefull when doing this. Since substantial part of all the true-matching tracks give Λ^0 and Λ_b mass that

IDSCAN setting	Vertexing	Trigger efficiency	Background rejection
1	w/o vertexing	$(7.3 \pm 0.4)\%$	$(97.9 \pm 0.2)\%$
	Di-muon vertexing	$(7.3 \pm 0.4)\%$	$(98.2 \pm 0.2)\%$
	Di-muon and Λ^0 vertexing	$(4.8 \pm 0.4)\%$	$(99.6 \pm 0.1)\%$
2	w/o vertexing	$(9.4 \pm 0.5)\%$	$(97.9 \pm 0.2)\%$
	Di-muon vertexing	$(9.4 \pm 0.5)\%$	$(98.2 \pm 0.2)\%$
	Di-muon and Λ^0 vertexing	$(6.1 \pm 0.4)\%$	$(99.6 \pm 0.1)\%$
3	w/o vertexing	$(9.1 \pm 0.5)\%$	$(97.9 \pm 0.2)\%$
	Di-muon vertexing	$(9.1 \pm 0.5)\%$	$(98.2 \pm 0.2)\%$
	Di-muon and Λ^0 vertexing	$(6.6 \pm 0.4)\%$	$(99.6 \pm 0.1)\%$

Table 6.2: Efficiencies and background rejection factors of the trigger with the full Λ^0 reconstruction.

already pass the tight cuts, by loosening them we only include more and more random combinations of tracks that give Λ^0 and Λ_b mass only by chance. Of course, one could argue that this is not in fact a problem since we don't care why our signal event was taken but only that it happened so. Even though this is strictly speaking true, our concern is that the value of the efficiency of such a loose selection will strongly depend on the accuracy of the Monte Carlo simulation and it can be very far from reality.

IDSCAN setting	Vertexing	Trigger efficiency	Background rejection
1	w/o vertexing	$(69 \pm 1)\%$	$(75.0 \pm 0.7)\%$
	Di-muon vertexing	$(68 \pm 1)\%$	$(76.4 \pm 0.7)\%$
2	w/o vertexing	$(72 \pm 1)\%$	$(74.3 \pm 0.7)\%$
	Di-muon vertexing	$(71 \pm 1)\%$	$(75.7 \pm 0.7)\%$
3	w/o vertexing	$(73 \pm 1)\%$	$(72.9 \pm 0.7)\%$
	Di-muon vertexing	$(72 \pm 1)\%$	$(74.3 \pm 0.7)\%$

Table 6.3: Efficiencies and background rejection factors of the trigger with the partial Λ^0 reconstruction.

For the trigger with the partial Λ^0 reconstruction the situation is different. A distribution of the pseudo-mass made using the proton and the muons true-matching tracks is shown in Figure 6.9. Λ^0 mass was assigned to the proton candidate track instead of the proton one to get the pseudo-mass closer to the real mass of Λ_b. Note that the pseudo-mass peak is shifted toward the lower values which is the consequence of the missing momentum carried away by the pion. The cuts were taken as 3σ range around the central value and they are

4.5 GeV $< M_{\mu^+\mu^-\mathrm{p}} <$ 6.4 GeV. Calculated efficiencies with respect to the level-2 di-muon trigger *mu6mu6* are listed in Table 6.3. The trigger efficiencies of this method are much higher, however we have paid for it with the lower background rejection factors.

6.3.2 Cut Optimisation

In the previous chapter we have calculated the trigger efficiencies for the cut values determined from the distributions of the true-matching tracks. It gave us an idea about the performance of the different methods, however, we would like to know how the efficiency will change if we vary some cuts and what is the maximal possible efficiency for a certain value of the background rejection factor. The method that allow us to find the optimal cut values is called *cut optimisation*.

It is based on a systematic scan of the configuration space of the cut variables. It means that we change the cut values in small steps and for each configuration we calculate the efficiency and the background rejection factor. Taking these two values as coordinates in two-dimensional space they fill a region that is bounded from above by the maximal possible value of the efficiency for a given background rejection factor. The points lying on the boundary represent the optimal cuts configurations.

We have performed the cut optimisation procedure for settings no. 1 and 2. Figure 6.10 shows the result of the scan for the setting no. 2, full Λ^0 reconstruction and both vertexings (left) and for the partial Λ^0 reconstruction with the di-muon vertexing (right). The plots for the other configurations are shown in Appendix A. The efficiencies calculated in the previous section are indicated by black triangles in the plots. Note that there is still some space for the optimisation. For instance for the method with the full Λ^0 reconstruction we can get higher efficiency and almost the same rejection factor if we loosen the invariant mass cuts and impose a cut on the quality of the di-muon vertex and Λ_b distance. The new optimal value of efficiency will be $(16.2 \pm 0.6)\%$ with the background rejection $(99.3 \pm 0.1)\%$.

From the right plot we see that 3σ mass window is too large for the method without the the full reconstruction since the background rejection is too low. By tightening the mass cut we can increase the background rejection at the price of loosing some efficiency.

There is no reason in going through all the possible configurations and corresponding efficiencies here. From now on we will do just with the information about the optimal values provided by Figure 6.10 and those in Appendix A without knowing the actual configuration of the cuts that led to them. Let us just comment on two points.

All the optimal efficiencies of the algorithm with the full Λ^0 reconstruction were obtained without the cuts on the impact parameters of the pion and proton. It means that these cuts are useless and there is no need to implement them in the trigger algorithm. The good message from this is that it simplifies the algorithm. For the method with the partial Λ^0 reconstruction this cut improves the

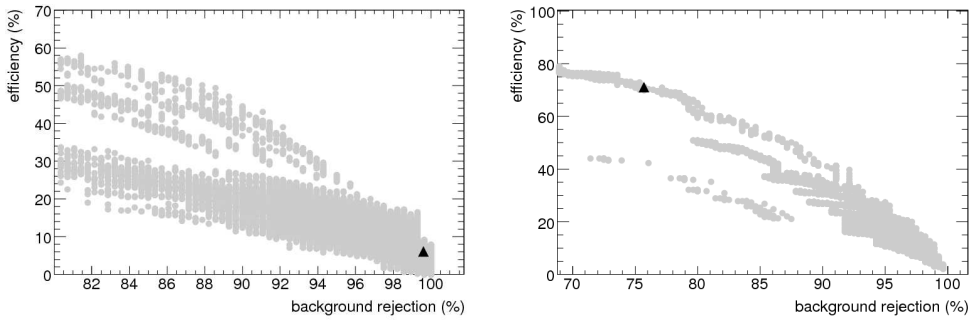

Figure 6.10: Results of the cut optimisation scan for the method with the full Λ^0 reconstruction and both vertexings (left) and the method with the partial reconstruction and the di-muon vertexing (right). IDSCAN configuration no. 2 was used for both plots.

performance since it is another criterion we can use for the background rejection.

Another point, to which we would like to draw your attention, is a relatively high efficiency of the method with the full Λ^0 reconstruction when we loosen the mass cuts. This was already mentioned in the previous section. If we look at the efficiencies for the rejection factor – for example – 82%, we see that the efficiencies of the method with and without the full Λ^0 reconstruction are basically the same (58.0% and 58.2%).

However, when we look at the cuts configurations we find out that the first efficiency corresponds to the configuration with all cuts opened except for the one on Λ_b mass: 4.7 GeV $< M_{\mu^+\mu^-p\pi} <$ 6.5 GeV. This means that the event is accepted if there are two opposite-charged tracks going to a common vertex (but no cut on χ^2 of the fit is applied) and in combination with the muons they give approximately Λ_b mass. Because we already know that the reconstruction probability of the hadronic final state is low (16%), it is safe to assume that the most of these tracks belong to some other particles and they are accepted only because of a rather large Λ_b mass window. These particles are produced together with Λ_b baryon in some QCD process, their momentum is moreless parallel to the one of Λ_b and thus they get reconstructed in the inner detector region around the muons. It is important to realise that properties of these particles are strongly dependent on the used Monte Carlo model. It can easily happen that in reality there will be a different number, distribution or composition of these particles in the signal or in the background processes and the the trigger selection based on such a selection will go all wrong.

On the other hand, the configuration of the second method is much more reasonable: Λ_b pseudo-mass 5 GeV $< M_{\mu^+\mu^-p} <$ 6.1 GeV and the quality of the di-muon vertex $\chi^2 < 10$. Of course it can still happen that the signal event will be triggered by chance and not by the presence of the studied process, however when looking at the distribution of $M_{\mu^+\mu^-p}$ in Figure 6.9 and taking into account

the proton reconstruction efficiency (75%) it is safe to assume that the substantial part of the events was accepted because of the presence of the final state proton.

The conclusion from this analysis is that each method is suitable for a selection with different required background rejections. If a low background rejection can be used (rejection factor $< 90\%$), the method with the partial reconstruction is better. If a high background rejection is required ($> 99\%$), the method with the full reconstruction starts to really select the studied process and its performance will be better than the one of the partial reconstruction method.

6.3.3 Rate Estimates

A di-muon trigger rate originate in the physics processes where two muons are present in the final state. The rate of i-th process can be calculated as:

$$R_i = \mathcal{L} \int \frac{d^2\sigma_i}{dp_{\mathrm{T}}^{(1)} dp_{\mathrm{T}}^{(2)}} \, \epsilon(p_{\mathrm{T}}^{(1)}, p_{\mathrm{T}}^{(2)}) \, dp_{\mathrm{T}}^{(1)} dp_{\mathrm{T}}^{(2)}, \tag{6.4}$$

where $\mathcal{L}$ is the beam luminosity, $d^2\sigma_i/dp_{\mathrm{T}}^{(1)}dp_{\mathrm{T}}^{(2)}$ is the differential cross section of i-th process as a function of the muons transverse momenta and $\epsilon(p_{\mathrm{T}}^{(1)}, p_{\mathrm{T}}^{(2)})$ is the di-muon trigger efficiency. Processes that significantly contribute to the di-muon rate are listed in Table 6.4 (taken form [13]). In the previous sections we have presented the background rejection factors for the first process. The rejection factor of the other two processes can be different since the distributions of the final state muons differ from the distributions of the first process. However, because the simulation with the other two processes haven't been done, we will assume that the rejection factors of all three processes are the same and we will just sum up the rates. This assumption is somewhat pessimistic, since muons decayed from charmed hadrons are softer than those decayed from bottom hadrons. Thus in this study we use lower rejection factors than we would get from the proper simulation.

Process	Cross section	Rate (Hz)	
		10^{33} cm^{-2}s^{-1}	10^{34} cm^{-2}s^{-1}
$b\bar{b} \to \mu^+\mu^-X$	110.5 nb	110.5	1105
$c\bar{c} \to \mu^+\mu^-X$	248.0 nb	248.0	2480
$J/\psi \to \mu^+\mu^-$	32.8 nb	32.8	328
Total	391.3 nb	391.3	3913

Table 6.4: Cross sections and rates of di-muon processes. The values correspond to the events after the generator pre-selection requiring $p_{\mathrm{T}}(\mu_{1(2)}) > 6(4)$ GeV, $|\eta(\mu)| < 2.5$. The values were taken from [13].

An efficiency of the proposed trigger algorithm can be expressed as a product of the level-2 di-muon trigger efficiency and the efficiency of the b-physics hypoth-

esis part with respect to the events accepted by the level-2 di-muon trigger. The first efficiency doesn't change with different settings while the latter one does. That is the reason why in the previous sections we have expressed the efficiencies with respect to the di-muon trigger one. The level-2 di-muon trigger *mu6mu6* efficiency was calculated using the background sample $b\bar{b} \rightarrow \mu^+\mu^-X$ and the signal sample $\Lambda_b \rightarrow \Lambda^0(p\pi)\mu^+\mu^-$. The efficiencies are 23.3% for the background and 32.2% for the signal.

The total output rate from the ATLAS level-2 trigger is expected to be 1–2 kHz and the rate allocated for b-physics will be 5–10% from the bandwidth. Taking our rough estimate of the di-muon trigger efficiency for the background, the rate from the di-muon trigger will be 91 Hz for luminosity of 10^{33} $cm^{-2}s^{-1}$ and 911 Hz for luminosity of 10^{34} $cm^{-2}s^{-1}$, however in reality this value will be higher since a pile-up of $\sim$23 interactions per one bunch crossing must be taken into account.

The ATLAS b-physics program is planned for 10^{33} $cm^{-2}s^{-1}$ luminosity run. However, we investigate the performance also for the nominal luminosity, even though at a present time it is not clear whether there will be a trigger rate allocated for the b-physics at the nominal luminosity run.

If we reserve 0.05% of the level-2 bandwidth to this trigger it means that we must reduce the background rate to 0.5 Hz which corresponds to the rejection factor of approximatelly 99.4% for the lower luminosity and about 99.9% for the nominal one. The optimal efficiencies, background rejection factors and the signal rates for the trigger configurations that fill up 0.05% of the level-2 trigger rate bandwidth are shown in Table 6.5. The value of the cross section of the process $pp \rightarrow X + \Lambda_b(\rightarrow \Lambda(p\pi)\mu^+\mu^-)$ was taken from [11]. In reality, the reserved rate may be higher because of an overlap of the background rates from the different triggers. If the background events are accepted by more triggers the total rate will be lower than a sum of the background rates of the individual triggers.

Luminosity ($cm^{-2}s^{-1}$)	Λ^0 reco.	B. rejection w.r.t. *mu6mu6*	Efficiency w.r.t *mu6mu6*	Efficiency w.r.t. truth	Signal rate (μHz)
10^{33}	Full	99.4%	16.5% (12.9%)	5.3% (4.2%)	63 (50)
10^{33}	Part.	99.4%	6.0% (8.0%)	1.9% (2.6%)	21 (31)
10^{34}	Full	99.9%	8.0% (6.0%)	2.6% (1.9%)	310 (210)

Table 6.5: Background rejections, efficiencies and signal rates. The triggers with the vertexing were used. Numbers in parenthesis correspond to the reconstruction done by the IDSCAN setting no. 1 while the numbers outside the parenthesis to the IDSCAN setting no. 2. The errors of the signal efficiencies are of the order of 0.5–1%.

For the chosen background rejection factors the best performance can be achieved using the trigger with the full Λ^0 reconstruction and both vertexings.

For the integrated luminosity of 30 fb^{-1} such a trigger will collect about 1900 events which is statistics expected to be collected after 3 years of running at the luminosity of 10^{33} $cm^{-2}s^{-1}$. Such a statistics corresponds to the one expected to be gained after the offline selection as mentioned in Chapter 4.2. At the nominal luminosity, the trigger would collect about 2680 signal events per 100 days, which is approximately 1 year of the LHC operation. However, at the nominal luminosity there will be in average 23 interactions per a bunch-crossing thus the background rate will be probably higher than estimated here.

Uncertainties in rate predictions are dominated by an uncertainty of b-production cross section predictions at LHC energy, which is considered to be uncertain by a factor of two [21]. Estimated rates for the other rare decays and the methods based on the single RoI approach will be presented in [11].

Chapter 7

Muon Trigger Calibration

Cross section measurements as well as searches for rare decays and many other b-physics measurements require a good understanding of the muon trigger efficiency and we must have a strategy for measuring it from ATLAS data. In this chapter a method how to measure single and di-muon efficiency using *tag-and-probe* method is described.

First let us explain several basic concepts. Each event containing some physical process that we are interested in has a certain probability that it will be triggered. This probability – or so called *trigger efficiency* – is typically lower than 100% which means that not all of the events will be recorded. When measuring cross sections, this inefficiency would lead to the lower values if the results weren't corrected. Also, a lot of measurements that compare distributions of measured quantities to the theoretical ones are sensitive to the trigger inefficiency since it can change the shape of the measured distributions.

Let us use the measurement of a polarisation of J/ψ particle as an illustrative example. The polarisation of J/ψ particle depends on the production mechanism and the transverse momentum of J/ψ [10]. From data it can be measured for instance by analysing events with $J/\psi \to \mu^+\mu^-$ where the measured quantity will be a decay angle $\cos\theta^*$ of the positive muon in the J/ψ rest frame where z-axis is taken as a direction of J/ψ in the lab frame. The distribution of $\cos\theta^*$ is parametrised by the following formula:

$$\frac{d\Gamma}{d\cos\theta^*} \propto \left(1 + \alpha\cos^2\theta^*\right), \tag{7.1}$$

where a polarisation parameter $\alpha = 0$ for unpolarised J/ψ's, while $\alpha = +1$ and $\alpha = -1$ corresponds to a full transverse and longitudinal polarisation respectively [10]. For the sake of our simple example let's assume that J/ψ's are produced unpolarised and thus the measured $\cos\theta^*$ distribution should be flat. However, if a very simple selection is applied by requiring one muon to have p_{T} greater than 4 GeV and the other greater than 6 GeV, we obtain the distribution shown at Figure 7.1. This selection can represent explicit cuts on p_{T} imposed by a di-muon trigger. It is evident that the obtained distribution is far from being flat. The

drop of the distribution for the values close to ± 1 is caused by the fact that for these angles one of the muons flies in the opposite direction to J/ψ, therefore its momentum is lower and it is more likely to be rejected by $p_{\mathrm{T}} > 4(6)$ GeV requirement. If we try to fit the distribution with the theoretical Formula (7.1) we will definitely get the wrong value of the polarisation parameter α. The theoretical function must be corrected to the trigger inefficiency in order to get the right value.

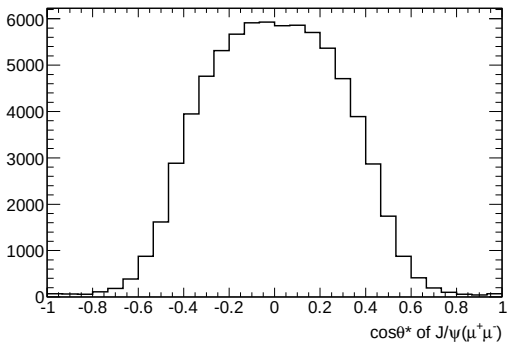

Figure 7.1: Distribution of the decay angle $\cos\theta^*$ of unpolarised J/ψ's when only events with the final state muons with p_{T} greater than 4 and 6 GeV were kept. The angular distribution of the whole sample would be flat.

Another important thing one must realise is that the trigger efficiency is a function of all the parameters that completely describe the event. These parameters don't necessary need to be only the ones that describe our measured process. As an example we will use again the process J/$\psi \to \mu^+\mu^-$, but this time J/ψ will be a decay product of some B hadron. One could easily jump to a conclusion that the probability of this event to be triggered by a di-muon trigger is fully determined by the final state of J/ψ decay. However, there will be another B hadron (which contains a charge conjugated b-quark) present in the event since flavour – in this case *bottomness* – is conserved in strong interactions and thus b-quarks are produced in quark-antiquark pairs ($\mathrm{b\bar{b}}$). This second B hadron have quite a large probability to decay into a final state containing a muon [23]. Estimated cross sections for process $\mathrm{pp} \to \mathrm{X} + \mathrm{b}(\to \mu\mathrm{X})$ at LHC energy are plotted in Figure 3.4. A presence of this third muon will also influence the probability of the event to be triggered. Simply speaking, it can happen that the event is accepted by the trigger even though it wouldn't be if there were just the final state muons from J/ψ.

Let $\epsilon^{1\mu}(p_{\mathrm{T}}, \eta, \phi)$ is the probability that the muon will be reconstructed by the trigger reconstruction algorithm with some explicit cut on the transverse momentum (*single-muon trigger reconstruction efficiency*). p_{T}, η and ϕ are the transverse momentum, pseudorapidity and azimuthal angle of the muon. Then

$$\epsilon^{2\mu}(p_{\mathrm{T}}^{(1)}, \eta^{(1)}, \phi^{(1)}, p_{\mathrm{T}}^{(2)}, \eta^{(2)}, \phi^{(2)}) = \epsilon^{1\mu}(p_{\mathrm{T}}^{(1)}, \eta^{(1)}, \phi^{(1)}) \times \epsilon^{1\mu}(p_{\mathrm{T}}^{(2)}, \eta^{(2)}, \phi^{(2)}) \quad (7.2)$$

will be the probability that two muons parametrised by $p_{\mathrm{T}}^{(1,2)}$, $\eta^{(1,2)}$, $\phi^{(1,2)}$ will be reconstructed by the trigger reconstruction algorithm. Formula (7.2) is valid under a condition that the single-muon reconstruction efficiencies are uncorrelated. This is not strictly speaking true, because the di-muon reconstruction efficiency drops when the muons are close, i.e. $\Delta R < 0.2$. This effect is discussed later in Chapter 7.3.3, here we will assume that Formula (7.2) is valid in the whole range of the kinematic parameters. Having the efficiency $\epsilon^{1\mu}$ we can calculate the probability that the event containing our process will be triggered by a di-muon trigger:

$$\epsilon_{event} = 1 - \prod_i (1 - \epsilon_i) - \sum_i \epsilon_i \prod_{j \neq i} (1 - \epsilon_j), \tag{7.3}$$

where $\epsilon_i = \epsilon^{1\mu}(p_{\mathrm{T}}^{(i)}, \eta^{(i)}, \phi^{(i)})$ and indices i and j runs over all the muons in the event. A derivation of Formula (7.3) is easy: the second term corresponds to the probability that no muon will be reconstructed and the third one to the probability that just one muon will be reconstructed. By subtracting these terms from 1 we get the probability that two or more muons will be reconstructed by the trigger algorithm and thus the event will pass the di-muon trigger. Note that ϵ_{event} is a function of the kinematic parameters of all the muons in the event. To get a total trigger efficiency for some process, one must integrate over all kinematic variables:

$$\epsilon_{total} = \int \dots \int \prod_i dp_{\mathrm{T}}^{(i)} d\eta^{(i)} d\phi^{(i)} f^{(i)}(p_{\mathrm{T}}^{(i)}, \eta^{(i)}, \phi^{(i)}) \epsilon_{event}, \tag{7.4}$$

where $f^{(i)}(p_{\mathrm{T}}^{(i)}, \eta^{(i)}, \phi^{(i)})$ are distributions of the single-muon kinematic variables. Usually we need to calculate the efficiency as a function of some other kinematic variables – for instance p_{T}, η and ϕ of the mother particle. In this case we just add Dirac delta-function of form $\delta[X - X(p_{\mathrm{T}}^{(i)}, \eta^{(i)}, \phi^{(i)})]$ to the integral. Here $X = X(p_{\mathrm{T}}^{(i)}, \eta^{(i)}, \phi^{(i)})$ is the new variable calculated from the old ones.

From what was written above it seems that there is practically unlimited number of parameters that one needs to fully describe the muon trigger efficiency of a certain process. In addition to the final state muons of the studied process there can be 'combinatorial' muons decayed from other b- and c-hadrons, as well as muons decayed from pions and kaons, $\mu^+\mu^-$ pairs produced by Drell-Yann mechanism, etc. However, ATLAS high-level trigger provides a number of mechanisms that reduce the influence of these other muons. There is a rejection of muons from pions and kaons implemented in the muon reconstruction algorithms [8]. Application of invariant mass cuts and a vertexing in trigger hypothesis algorithms significantly reduces the number of fake (combinatorial) signatures of the studied process. Also, the event rate drops rapidly with the multiplicity of muons. Figure 3.4 shows that the estimated rate of di-muon events is approx. two orders of magnitude lower than the single-muon rate. All this implies that for the most of the cases one can calculate just with the final state muons of the studied process and neglect the effect of other muons in the event.

Using the assumption from the previous paragraph we can calculate di-muon efficiency of J/ψ by simplifying Formula (7.4):

$$\epsilon^{\mathrm{J}/\psi}(p_{\mathrm{T}}^{\mathrm{J}/\psi}, \eta^{\mathrm{J}/\psi}, \phi^{\mathrm{J}/\psi}) = \iint d\cos\theta^* d\phi^* f(\cos\theta^*) \times$$
$$\times \epsilon^{\mu^+}(p_{\mathrm{T}}^{\mathrm{J}/\psi}, \eta^{\mathrm{J}/\psi}, \phi^{\mathrm{J}/\psi}, \cos\theta^*, \phi^*) \times \epsilon^{\mu^-}(p_{\mathrm{T}}^{\mathrm{J}/\psi}, \eta^{\mathrm{J}/\psi}, \phi^{\mathrm{J}/\psi}, \cos\theta^*, \phi^*), \tag{7.5}$$

where $\cos\theta^*$ is the polar decay angle of the muons (defined above) and ϕ^* is the azimuthal one. $f(\cos\theta^*)$ is the distribution of the polar decay angle. Distribution of the azimuthal one is flat, hence the choice of the direction from which it will be measured is arbitrary and doesn't change the result. The trigger algorithm reconstruction efficiencies ϵ^{μ^+} and ϵ^{μ^-} are expressed as functions of the new kinematic variables $p_{\mathrm{T}}^{\mathrm{J}/\psi}$, $\eta^{\mathrm{J}/\psi}$, $\phi^{\mathrm{J}/\psi}$, $\cos\theta^*$ and ϕ^*. The original six single-muon kinematic variables can be calculated from the new ones and the value of J/ψ mass.

Often, the function $f(\cos\theta^*)$ is not known and is the subject of the measurement. Then one must express Formula (7.5) in a more general form, where $\cos\theta^*$ is not integrated out:

$$\epsilon^{\mathrm{J}/\psi}(p_{\mathrm{T}}^{\mathrm{J}/\psi}, \eta^{\mathrm{J}/\psi}, \phi^{\mathrm{J}/\psi}, \cos\theta^*) = \int d\phi^* \epsilon^{\mu^+}(p_{\mathrm{T}}^{\mathrm{J}/\psi}, \eta^{\mathrm{J}/\psi}, \phi^{\mathrm{J}/\psi}, \cos\theta^*, \phi^*) \times$$
$$\times \epsilon^{\mu^-}(p_{\mathrm{T}}^{\mathrm{J}/\psi}, \eta^{\mathrm{J}/\psi}, \phi^{\mathrm{J}/\psi}, \cos\theta^*, \phi^*). \tag{7.6}$$

Note that Formula (7.6) is general and can be used to calculate the di-muon efficiency of any process $A \to \mu^+\mu^-$ (still under a condition that we can neglect the effect of other muons from parallel processes). To calculate efficiency of $\mathrm{B} \to \mu^+\mu^-\mathrm{X}$ we must introduce another variable – e.g. a mass of the muon system $M_{\mu^+\mu^-}$ – to fully describe the process. This is the case of the process $\Lambda_\mathrm{b} \to \mu^+\mu^-\Lambda^0$ that is discussed in Chapter 6.3.1.

7.1 Tag-and-probe Method

In the previous chapter we have discussed how to calculate trigger efficiencies when knowing the single-muon trigger reconstruction efficiency $\epsilon^{1\mu}$. However, the latter efficiency is not known and it must be either measured or calculated using the Monte Carlo simulation of the ATLAS detector. At the design-time of the ATLAS experiment, Monte Carlo simulations are used to calculate trigger efficiencies and rates. Once LHC will start producing data, we want to measure it from real data since simulations can be wrong.

In order to measure $\epsilon^{1\mu}$, we must collect an unbiased sample of muons. Because the sample will be always finite, the obtained distribution of kinematic parameters will have to be made in a finite binning. We designate $N(p_\mathrm{T}, \eta, \phi)$ the number of muons in the bin where p_T, η and ϕ fall. If the statistics is large enough, we can estimate the reconstruction efficiency as a ratio

$$\epsilon^{1\mu}(p_\mathrm{T}, \eta, \phi) \approx \frac{N_{\mathrm{trig}}(p_\mathrm{T}, \eta, \phi)}{N(p_\mathrm{T}, \eta, \phi)}, \tag{7.7}$$

where $N_{\text{trig}}(p_{\text{T}}, \eta, \phi)$ is the number of muons reconstructed by the trigger reconstruction algorithm in the bin around p_{T}, η and ϕ.

This calculation – however simple it may look – is in fact quite difficult to make. First of all, the function $N(p_{\text{T}}, \eta, \phi)$ corresponds to the distribution of the real muons, which is never known. The only information that we have is the outcome of some measurement. In this case it will be the muon track reconstructed by the ATLAS offline reconstruction algorithms. These algorithms have their own efficiencies that must be measured or calculated from Monte Carlo simulations. It is not the goal of this thesis to study the efficiency of the offline reconstruction algorithms, thus from now on we will express all the efficiencies with respect to the offline reconstruction. Also all the kinematic variables will be the parameters of the offline-reconstructed tracks (which can naturally differ from the true ones). Formula (7.7) will then change to:

$$\epsilon^{1\mu}(p_{\text{T}}, \eta, \phi) \approx \frac{N_{\text{trig}}(p_{\text{T}}, \eta, \phi)}{N_{\text{off}}(p_{\text{T}}, \eta, \phi)}, \tag{7.8}$$

where $N_{\text{off}}(p_{\text{T}}, \eta, \phi)$ is the number of offline-reconstructed muon tracks in the bin around p_{T}, η and ϕ. For the sake of simplicity we use the same designation for the single-muon efficiency in Formula (7.7) and (7.8) even though they correspond to different quantities.

Another issue is how to collect the unbiased muon sample. The high event rates don't allow us to collect the sample with the trigger being switched off. On the other hand if we use a muon trigger to collect our sample it won't be unbiased since all the events will contain some muon which was reconstructed by the trigger algorithm. The method that allow us to get the unbiased sample of muon tracks using the single-muon trigger is called *tag-and-probe* and its principle can be explained as follows:

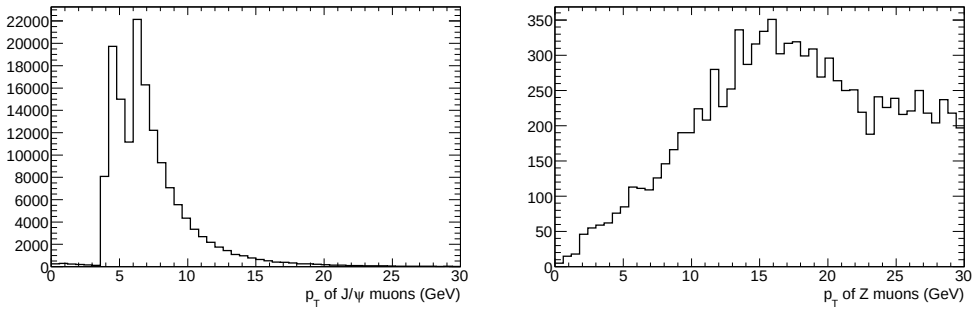

Figure 7.2: Distribution of the transverse momentum of J/ψ final state muons (left) and Z final state muons (right) from used Monte Carlo samples. The two peaks visible in the left figure corresponds to $p_{\text{T}} > 4(6)$ GeV cuts that were applied on J/ψ muons at the generator level in the Monte Carlo simulation.

The sample of events is collected using some single-muon trigger, requiring

one trigger muon candidate with p_{T} above a certain threshold. The tag-and-probe method exploits the fact, that in the sample there will also be events containing two muons. These events will be usefull for our trigger calibration. Furthermore, we restrict the di-muon events in our sample to only those where the muons are decay products of quarkonia J/ψ and Υ or an intermediary boson Z. These events will be identified by the offline reconstruction and analysis algorithms (see for instance [10]). We require this for one reason: there is always some fraction of *fake* offline muon tracks i.e. tracks that don't correspond to any real particle. By requiring that the muon tracks form J/ψ particle we reject significant part of these fake tracks from our analysis. However, the method itself could work as well with any di-muon events.

For a low-p_{T} muon trigger calibration events with J/ψ decay are ideal since the muon p_{T} spectrum peaks toward lower values (see Figure 7.2). On the other hand, Z-boson events are useful for calibrations of high-p_{T} triggers. In our study we use J/ψ events for the efficiency calibration, however, the method remains the same for other di-muonic decay channels.

Once we have our J/ψ muons identified by the offline analysis, we check which one of them was reconstructed by the trigger reconstruction algorithm. This muon is called the *tag* muon and it is the one that caused the event to be accepted by the single-muon trigger. The second muon – called the *probe* muon – has not contributed to the trigger decision. It may or may not be reconstructed by the trigger algorithm with the probability that is uncorrelated to the trigger reconstruction efficiency of the first muon. Therefore the sample of probe muons will be unbiased and we can use it to calculate the trigger reconstruction efficiency $\epsilon^{1\mu}$ using Formula (7.8).

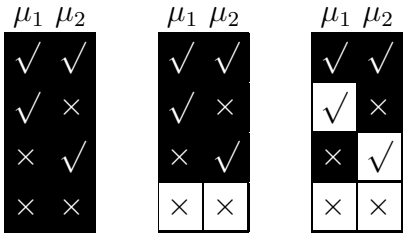

Figure 7.3: Selection of the probe muons. Reconstructed muons are indicated by $\surd$-sign, not-reconstructed ones by $\times$-sign. Muons used for the single-muon reconstruction efficiency calculation are marked by a black colour. In the original sample (left) all the muons are used. After the trigger selection (middle), events with both muons not-reconstructed are not taken. The tag-and-probe method selects an unbiased sample of muons from the sample taken by the trigger (right).

The process of the probe muons selection is illustrated in Figure 7.3. The left chart represents the sample of all J/ψ muons. There is some fraction of events where both muons were reconstructed by the trigger algorithm, some fraction of events where either first or the second muon was reconstructed and finally

some fraction where none of the muons is reconstructed. If we use the single-muon trigger to collect the sample of J/ψ's, we will exclude the events where no muons were reconstructed. This is illustrated in the middle chart by leaving the bottommost fields white. It is evident that if we use such a sample to calculate the efficiency we will get a wrong value. The sample of probe muons is represented by the right chart. The tag-and-probe method checks the reconstructed muon and includes the other one into the sample of probe muons. It means that if both muons were reconstructed then both will be included into the sample since both can be considered as tag but also as probe muons. On the other hand, if only one of the muons is reconstructed, it won't be included into the sample while the not-reconstructed one will. By looking at the chart we see that the ratio of reconstructed and not-reconstructed muons used for the calibration (black fields) is again the same as in the original sample.

7.2 Calibration Trigger Requirements

In order to calculate the function $\epsilon^{1\mu}$ with a high enough precision, one must have large statistics to be able to use a fine binning while preserving a relatively high number of events in each bin. This requirement can be satisfied with the following selection criteria at each trigger level [9]:

Level-1: Single muon trigger with p_{T} above a certain threshold.

Level-2: J/ψ reconstruction within one RoI using the TrigDiMuon algorithm (see [9] for details) to enhance J/ψ events. The second muon in the event will be find among inner detector tracks reconstructed within the extended region around the first muon candidate. For this second track, no (or very limited) information from the muon spectrometer must be used in order to collect an unbiased sample. J/ψ fraction of the collected events will be enhanced by combining the inner detector tracks with the first muon candidate and an application of the cut on J/ψ invariant mass.

Event filter: Pass-through.

Given the event filter output rate of $\sim$ 100 Hz [2] it is reasonable to reserve a few Hz of the bandwidth for this calibration trigger. Any time before ATLAS starts to collect data the trigger rates are an unknown variable and all the estimates suffer from the great uncertainties of cross sections. Thus it is too soon to make any definitive statements on what selection thresholds and prescale factors should be. Some estimates of the overall rate and the fraction of J/ψ's selected by this trigger were made in [9] using Monte Carlo simulations. The rates after each selection level together with the contribution of J/ψ are shown in Table 7.1. Assuming that we want to allocate rate of 1 Hz for the calibration trigger, we must apply a prescale factor of 3 to reduce the rate. Then the J/ψ event rate

will be 0.06 Hz. With an integrated luminosity of 100 pb^{-1} we collect about 3×10^5 events. Such a statistics is expected to be collected after the first year of data-taking.

	Rate (Hz)	J/ψ rate (Hz)	J/ψ fraction
Level-1	380	0.21	0.05%
Level-2	3	0.19	6%

Table 7.1: The calibration trigger rates after level-1 and level-2 for a luminosity of $10^{31}\text{cm}^{-2}\text{s}^{-1}$ with $p_{\text{T}} > 6$ GeV threshold. The contribution of $\text{J}/\psi \to \mu^+\mu^-$ process to the rate is also shown.

In this study we don't apply any explicit cuts on p_{T} of the calibration trigger in order to have as large sample of the probe muons as possible. However, there is an implicit cut given by the reconstruction efficiency of the algorithm which is around 2 GeV [9]. The results of of the tag-and-probe method don't depend on the value of the calibration trigger p_{T} threshold.

7.3 Performance Studies

7.3.1 Trigger Reconstruction Efficiency

In this chapter we study a performance of the tag-and-probe method using Monte Carlo samples. We use the reconstructed data samples (see Chapter 5) that contain information about tracks reconstructed by the offline reconstruction algorithms [1] as well as the trigger objects (level-1 RoI's and level-2 tracks) reconstructed by the trigger algorithms [2]. We call the muon tracks reconstructed by the offline algorithms *offline muon tracks* (or simply *offline muons*) and ones reconstructed by the trigger algorithms *trigger muon tracks*. The MuComb algorithm [8, 28] was used in this study for the trigger reconstruction, but the method works in the same way for any other trigger reconstruction algorithm.

In order to determine whether a certain offline muon was reconstructed also by the trigger algorithm, we need to match it to the trigger object, i.e. a level-1 RoI and a level-2 trigger track. A distance $\Delta R = \sqrt{\Delta\eta^2 + \Delta\phi^2}$ between the offline track and the trigger object in $\eta \times \phi$ plane was used for the matching. At level-2 the matching is simple since parameters of both the offline and the trigger tracks are expressed at the perigee of the track. At the level-1 the situation is more complicated since position is taken as a centre of the RoI in the muon spectrometer. Because of the magnetic field the track of the muon is curved, thus η and ϕ at the track perigee are different from those in the muon spectrometer. The *track extrapolator* – a tool that can extrapolate tracks from the inner detector to the muon spectrometer – had to be used to extrapolate the track to the pivot

plane of RPC or TGC chamber before ΔR between the offline track and the RoI was calculated.

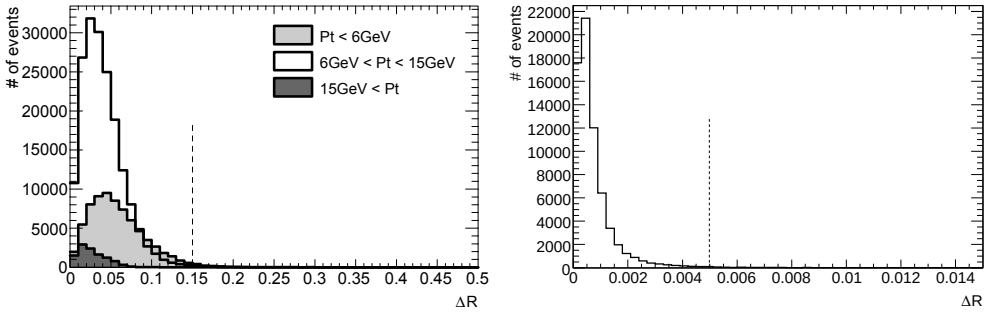

Figure 7.4: Distribution of the distance ΔR between the offline muon track and the muon RoI (left) and the trigger muon track (right). The cuts are indicated by the vertical dashed lines.

Figure 7.4 shows the distributions of ΔR between the offline tracks and the trigger objects. RoI was considered to be matching the offline track if $\Delta R < 0.15$ while the trigger track was considered to be matching the offline one if $\Delta R < 0.005$.

Once the matching criteria are established the distributions $N_{\text{off}}(p_{\text{T}}, \eta, \phi)$ and $N_{\text{trig}}(p_{\text{T}}, \eta, \phi)$ can be created and the trigger reconstruction efficiency $\epsilon^{1\mu}$ can be calculated using the probe muons and Formula (7.8). Depending on what we choose for N_{trig} we get different efficiencies. If we use number of all the offline muons matching some level-1 RoI we get a level-1 reconstruction efficiency. Note that since there is a number of different thresholds available at level-1, there will be a number of different level-1 reconstruction efficiencies. However, J/ψ events are suitable only for the calibration of triggers with low-p_{T} thresholds (4 GeV, 6 GeV and 8 GeV). In this thesis we study only the case of 6 GeV threshold.

For level-2 efficiencies, a distribution of all the offline muons matching a level-1 RoI and also a level-2 muon trigger track was taken as N_{trig}. This time there are many more possibilities how to set the thresholds since all the combinations of level-1 and level-2 thresholds can be used. In this study we use the set of thresholds designated as *mu6* which are the thresholds designed to efficiently select muons with $p_{\text{T}} \geq 6$ GeV. We denote the efficiency $\epsilon^{1\mu}$.

In order to check that the selection of the probe muons was really unbiased we have created the *reference sample* of muons by taking all the offline reconstructed J/ψ muons in all available events. Since the probe muon sample is an unbiased subset of the reference sample all the results made using both samples should correspond. Figure 7.5 shows the comparison of an overall trigger reconstruction efficiency as a function of p_{T} obtained using both samples. To calculate the overall efficiency, the distributions $N_{\text{trig}}(p_{\text{T}}, \eta, \phi)$ and $N_{\text{off}}(p_{\text{T}}, \eta, \phi)$ were integrated over

η and ϕ and then divided. Figure 7.5 shows that both functions agree well which means that we have a good sample of probe muons.

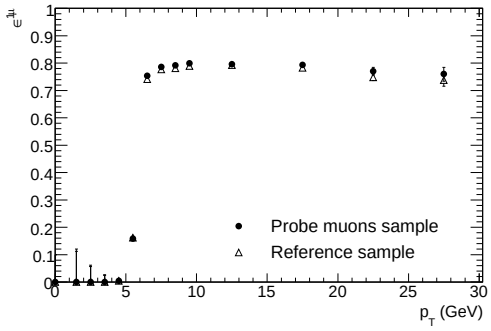

Figure 7.5: Comparison of an overall trigger reconstruction efficiency as a function of p_{T} calculated using the probe muons and the reference sample.

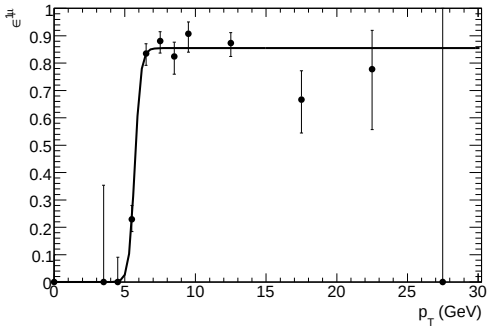

Figure 7.6: Example of the level-2 trigger reconstruction efficiency calculated using the probe muons sample in one $\eta \times \phi$ bin. Points were fitted with the function (7.9).

A special attention must be given to the choice of the binning in η and ϕ. The single-muon trigger reconstruction efficiency is not homogeneous because there are areas where muon chambers are missing to make space for the calorimeter support poles and cables and in some regions p_{T} determination is not good due to a complicated shape of the magnetic field [6]. Thus it is desirable to have as fine binning as possible to reflect all the changes in the efficiency. On the other hand, we are limited by the size of the statistics.

In the barrel region ($|\eta| < 1.05$) $\eta \times \phi$ space was divided into 10 bins in η and 10 bins in ϕ. In end-cap region ($1.05 < |\eta| < 2.45$) one octant was divided into 10 bins in η and 6 bins in ϕ. All the octants were assumed to be identical thus they were superimposed and the entries were summed. The layout of the toroidal magnetic field is such that positive charged muons bend toward the beam axis on one side of the detector and outward on the other while for the negative muons it will be the other way around. The positive muons on one side will then behave the same way as the negative ones on the other and vice versa. For that reason two endcap distributions were created, one for $q\eta > 0$ and the other for $q\eta < 0$ (q is the charge of the muon). The layout of the endcap octants and the chosen binning is shown in Figure 7.7.

In each $\eta \times \phi$ bin, the efficiency is a function of p_{T} and it is evaluated in the centres of p_{T} bins. Because of the limited statistics the values suffer from rather large statistical errors. To reduce the influence of the statistical errors the values were fitted with the function:

$$\epsilon(p_{\mathrm{T}}) = \frac{A}{1 + \exp[-a(p_{\mathrm{T}} - b)]}, \tag{7.9}$$

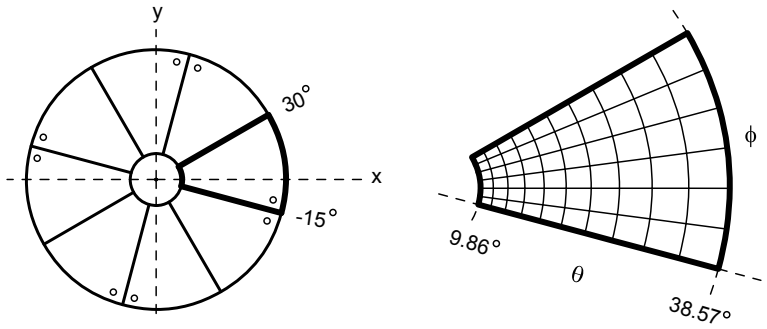

Figure 7.7: Layout of the endcap octants (left) and the chosen binning within one octant (right). The octants are not aligned with x-axis but they are rotated by $-15°$. Neighbouring octants are flipped. The bin size is constant in η so it is changing in θ as indicated in the right figure.

where A (*plateau height*), a (*slope*) and b (*shift*) are free parameters and they are different in each $\eta \times \phi$ bin. An example of such a fit for one bin in the barrel region is shown in Figure 7.6. Three smooth-like functions $A(\eta, \phi)$, $a(\eta, \phi)$ and $b(\eta, \phi)$ were created by interpolating the values of the parameters between the bin centres using the method of *Delaunay Triangles* [24]. We call the set of these three functions the *trigger efficiency map*. The corresponding plots are shown in Appendix B. Having this map, we can calculate the reconstruction efficiencies for any sample of muons. It is essential to realise that once this map is measured we don't need to rely on any Monte Carlo simulation of the ATLAS trigger system to calculate the trigger efficiency for the process we are interested in.

At last we will estimate errors and discuss limitations of the trigger efficiency map. Taking into account the number of bins and the estimated rates it is to be expected that we won't be able to fill each bin with hundreds of entries. This results into quite large statistical errors on calculated efficiencies as can be seen in Figure 7.6. These errors affect the accuracy of the fit. Errors on fit parameters were calculated using standard fitting tool of data analysis program ROOT [24]. The errors were interpolated between the bin centres the same way as the parameters themselves. Whenever the efficiency was calculated from the parameters using Formula (7.9) the error was estimated using the standard formula for the error propagation (see for instance [25]).

Average errors of the parameters are listed in Table 7.2. The parameter a has the largest error since it is the most sensitive to the quality of the fitted data. However, this parameter plays a more important role only in a turn-on region of the function (7.9) thus its uncertainty affects only a small amount of events. The most important parameter is A since it corresponds to the height of the plateau of the function (7.9). For a given statistics its relative statistical error is $\sim$6%. The statistical errors can be reduced by either collecting more events or by using

larger bins.

	Error of A	Error of a	Error of b
Barrel	5%	56%	2%
Endcap $q\eta > 0$	7%	41%	4%
Endcap $q\eta < 0$	6%	42%	4%

Table 7.2: Average relative statistical errors of the trigger efficiency map parameters.

Apart from the statistical errors there will be a number of systematic ones. By using ΔR matching we can overestimate or underestimate the reconstruction efficiency by choosing the cut that is not optimal. By assuming that all the barrel octants are identical we can miss drops of the efficiency caused by dead channels in some octants. Also, the tag-and-probe method can't take into account trigger fakes. It can happen that there is a level-1 RoI or a level-2 muon track that doesn't belong to any offline track. These cases are simply ignored. However, we assume that the most important contribution to the systematic error is the effect of the finite binning. The measured reconstruction efficiency is averaged over the bin which doesn't matter in the homogeneous regions but it does in regions where the efficiency changes rapidly.

We have estimated the systematic error by making a new trigger efficiency map with a finer $\eta \times \phi$ binning and subtracting it from the original one. The new binning was 15×15 in the barrel and 15×8 in the endcap regions. We have used the reference sample to create the new map in order to suppress statistical errors (the reference sample contains all the J/ψ muons). Average values of these estimates for the parameter A are listed in Table 7.3. It is important to realise that these values are only very rough estimates. Firstly, the new map has also a finite binning thus it suffers from the systematic error, too. Secondly, by subtracting the maps we add their statistical errors to our estimates. The largest systematic errors are in the regions where the muon chambers are missing and at the edge of the muon system. To get an idea how large these regions are we have calculated the area where the error is larger the 10% (see the third column of Table 7.3). By excluding these regions the average systematic error drops by a factor of 3.

To illustrate an accuracy of the trigger efficiency map predictions, we have created the projections of the trigger reconstruction efficiencies to p_{T}, η and ϕ-axis using the reference muon sample (see Figure 7.8). For each variable we superimpose two plots: one calculated using the distribution of the trigger-matching muons $N_{\mathrm{trig}}(p_{\mathrm{T}}, \eta, \phi)$ of our reference sample and Formula (7.8); the second using the trigger efficiency map. The calculation of the p_{T} projection using the map is straightforward. In each p_{T} bin we have calculated the efficiency as an average of the single-muon reconstruction efficiencies of all the offline muons that fall into that bin. The same way η and ϕ projections were made. The errors of the effi-

	Average syst. error	The area with error > 10%	Average error of the rest
Barrel	15%	31%	4%
Endcap $q\eta > 0$	13%	16%	4%
Endcap $q\eta < 0$	9%	20%	3%

Table 7.3: Average of the relative systematic errors of the parameter A. In the third column there is the fraction of the area where the systematic error is greater than 10%. Those are the regions where the efficiency changes rapidly. The average systematic error calculated without these regions is in the last column.

ciencies calculated from the map are a combination of the statistical errors and the systematic errors estimated using the method described in the previous paragraph. In the most regions the values correspond within a few %. The largest discrepancies can be seen in ϕ plot between -1 rad and -2 rad which is the bottom side of the detector.

7.3.2 Di-muon Trigger Efficiency of $J/\psi \to \mu^+\mu^-$

Decays of b-hadrons with J/ψ in the final state represent a very important b-physics channel. $J/\psi \to \mu^+\mu^-$ decay is a clear trigger signature because of a low backround and an excellent acceptance of the ATLAS muons system.

The simplest J/ψ trigger requires the presence of two muon candidates with p_{T} above a certain threshold. In addition it usually requires that the muons satisfy the cut on J/ψ invariant mass and to improve the combinatorial background rejection a vertex fitter can be used to reconstruct the decay vertex. In this section we use the trigger efficiency map to study the simple di-muon trigger efficiencies of $J/\psi \to \mu^+\mu^-$ events.

In Figure 7.9, J/ψ trigger efficiencies are shown. Firstly, we have used a simple di-muon trigger (designated as *mu6mu6*) that efficiently selects events with two muons with $p_{\mathrm{T}} > 6$ GeV and that was run when our J/ψ Monte Carlo samples were reconstructed. Thus for each event we had the information about which event was triggered. Using this information we have created the distributions of J/ψ transverse momentum $p_{\mathrm{T}}^{\mathrm{J}/\psi}$, pseudorapidity $\eta^{\mathrm{J}/\psi}$, azimuthal angle $\phi^{\mathrm{J}/\psi}$ and the distance of the final state muons $\Delta R^{\mathrm{J}/\psi}$ how they look like after the trigger selection. By dividing these distributions by the ones created without the trigger selection we have obtained the trigger efficiencies as a function of J/ψ variables. These efficiency curves are designated as the *reference efficiencies* in Figure 7.9.

Then we have created these distributions using the trigger efficiency map. To each event the probability that it will be triggered was assigned using Formula (7.3). In each $p_{\mathrm{T}}^{\mathrm{J}/\psi}$ bin of the efficiency curve, the value was calculated as an average of these probabilities. This procedure formally corresponds to the integration in Formula (7.4) where we have added $\delta[p_{\mathrm{T}}^{\mathrm{J}/\psi} - p_{\mathrm{T}}^{\mathrm{J}/\psi}(p_{\mathrm{T}}^{\mu^+}, \eta^{\mu^+}, \phi^{\mu^+}, p_{\mathrm{T}}^{\mu^-}, \eta^{\mu^-}, \phi^{\mu^-})]$

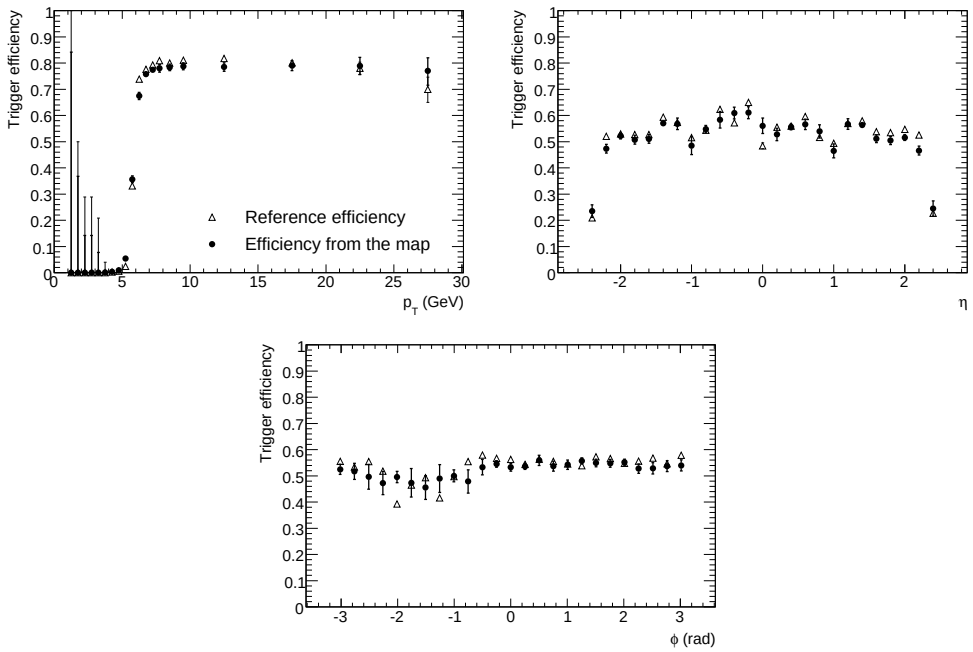

Figure 7.8: Projections of the single-muon reconstruction efficiencies to p_{T}, η and ϕ-axis. The *reference efficiency* was calculated using the distribution of the trigger-matching muons of the reference sample while the *efficiency from the map* was calculated using the trigger efficiency map.

Dirac delta-function to the right side. In Figure 7.9 these efficiencies are denoted as the *efficiency from the map*. An agreement of the two curves is within 7% in most regions except for some regions where the available statistics was low. The overall reference efficiency is 24.8% and the overall efficiency from the map is 25.4%.

The last paragraph of this section we devote again to the measurement of J/ψ polarisation. The measuremet is challenging because the trigger selection does not just change the shape of $\cos\theta^*$ distribution (see Figure 7.1) but also introduces a correlation between $\cos\theta^*$ and the other J/ψ variables. This can be easily understood by looking at Formula (7.6). In order to get the efficiency as a function of $\cos\theta^*$ we must integrate the formula over the other J/ψ variables:

$$\epsilon^{\mathrm{J}/\psi}(\cos\theta^*) = \int dp_{\mathrm{T}}^{\mathrm{J}/\psi} d\eta^{\mathrm{J}/\psi} d\phi^{\mathrm{J}/\psi} f(p_{\mathrm{T}}^{\mathrm{J}/\psi}, \eta^{\mathrm{J}/\psi}, \phi^{\mathrm{J}/\psi}) \epsilon^{\mathrm{J}/\psi}(p_{\mathrm{T}}^{\mathrm{J}/\psi}, \eta^{\mathrm{J}/\psi}, \phi^{\mathrm{J}/\psi}, \cos\theta^*), \tag{7.10}$$

where $f(p_{\mathrm{T}}^{\mathrm{J}/\psi}, \eta^{\mathrm{J}/\psi}, \phi^{\mathrm{J}/\psi})$ is the distribution of J/ψ variables. The trouble is that $f(p_{\mathrm{T}}^{\mathrm{J}/\psi}, \eta^{\mathrm{J}/\psi}, \phi^{\mathrm{J}/\psi})$ is model-dependent and can be even unknown. Issues of the polarisation measurement are discussed in [10] and we won't go through all the details here. Let us just mention few points. One way how to deal with the limited acceptance of di-muon trigger is to fit a Monte Carlo model-dependent templates

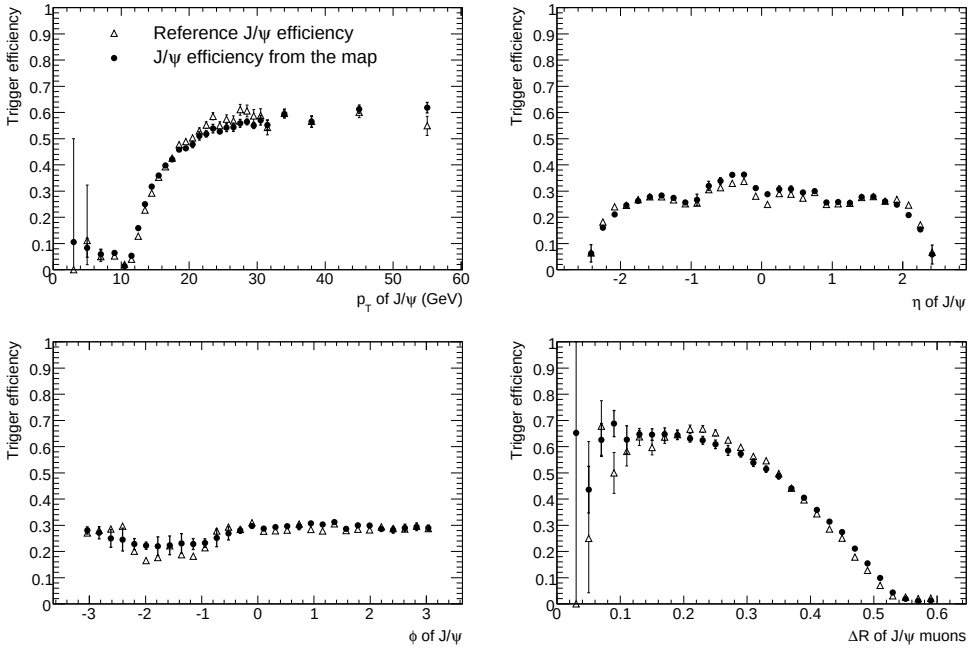

Figure 7.9: J/ψ trigger efficiency as a function of p_{T}, η, ϕ and ΔR of J/ψ. The *reference efficiency* was calculated using the information about the trigger decision while the *efficiency from the map* was calculated using the trigger efficiency map.

to the measured distribution. Another method proposed by the authors of [10] is to recover events with $\cos\theta^*$ close to ± 1 with a single-muon trigger with a high p_{T} threshold (*mu10*).

Figure 7.10 shows the trigger efficiency of the di-muon trigger (*mu6mu6*) as a function of $\cos\theta^*$ where we have required $p_{\mathrm{T}}^{\mathrm{J}/\psi} > 15$ GeV. The drop of efficiency for values close to ± 1 makes it difficult to distinguish between different models that predict J/ψ polarisation.

Figure 7.11 shows the trigger efficiency of the combination of the di-muon and the single-muon trigger (*mu6mu6 + mu10*). The efficiency of this trigger was calculated from the trigger efficiency map using the modification of Formula (7.3):

$$\epsilon_{event} = 1 - \prod_i (1 - \epsilon_i^{\mu 6}) - \sum_i (\epsilon_i^{\mu 6} - \epsilon_i^{\mu 10}) \prod_{j \neq i} (1 - \epsilon_j^{\mu 6}), \tag{7.11}$$

where $\epsilon_i^{\mu 6}$ and $\epsilon_i^{\mu 10}$ are the single-muon trigger reconstruction efficiencies with different thresholds. In derivation of the formula we have used the fact that when a muon is reconstructed by the algorithm with the threshold of 10 GeV it will be reconstructed by the one with 6 GeV threshold, too. The second term is then the probability that no muon is reconstructed by none of the algorithms and the third term corresponds to the probability that only one muon was reconstructed by the algorithm with 6 GeV cut, but it hasn't passed the 10 GeV one. By subtracting

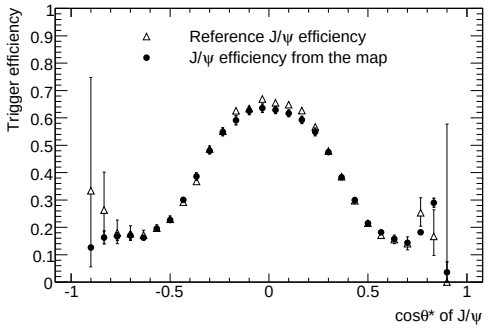

Figure 7.10: Di-muon trigger efficiency of J/ψ as a function of $\cos\theta^*$.

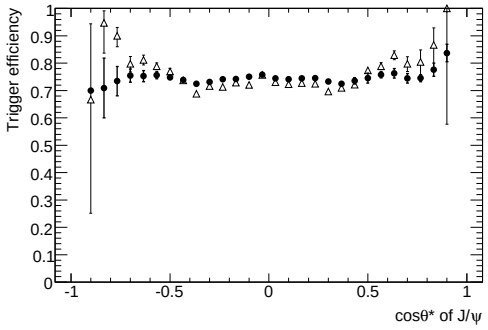

Figure 7.11: Trigger efficiency of the combination of the di-muon and the single-muon trigger as a function of $\cos\theta^*$.

these terms from 1 we get the probability that the event will be triggered by our trigger. Note that the trigger efficiency is now flat in a wide range of $\cos\theta^*$ and function (7.1) can be fitted directly to the measured data. A rather large discrepancy between the reference efficiency and the one from the map is caused by the fact that we didn't have a proper simulation of *mu10* trigger and we had to use its rough approximation. However, we can conclude that there isn't any huge disagreement between both methods.

7.3.3 Calibration of Rare B Decays Di-muon Trigger

In Chapter 4.2 we have mentioned the influence of the explicit p_{T} cuts on the forward-backward asymmetry. In this section we will use the full simulation of the di-muon trigger to investigate effects of the trigger selection. Also, we will show that the systematic errors of the trigger efficiency map doesn't have significant effect on the forward backward asymmetry.

The Monte Carlo sample of the process $\Lambda_{\mathrm{b}} \to \Lambda^0\mu^+\mu^-$ was used in this performance study. In order to see the effects of the di-muon trigger we must use as large statistics as possible. Therefore, we can't use the full offline analysis proposed in [11] to identify the signal process, since it rejects too many signal events. We have used the true information from the sample and true-matching offline muon tracks instead. The decay angle of the muons $\cos\theta^*$ was calculated as an angle between the positive true-matching offline muon track and the true Λ_{b} in the di-muon centre-of-mass system. This way we could use also the events where hadronic part of the final state wasn't reconstructed. The true-matching muons were required to have a common vertex in which the tracks parameters were evaluated.

Figure 7.12 shows the efficiency of the di-muon trigger *mu6mu6* as a function of the opening distance ΔR of the muons and as a function of the di-muon

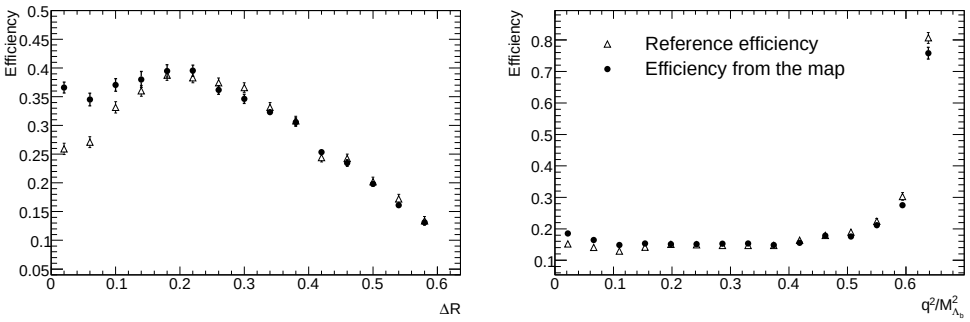

Figure 7.12: Efficiency of the di-muon trigger *mu6mu6* as a function of the opening distance ΔR of the muons (left) and as a function of q^2 (right).

invariant mass $q^2 = M^2_{\mu\mu}$. Again, the efficiencies were calculated using the information about the trigger decision (reference efficiency) and using the trigger efficiency map (efficiency from the map). Note that the reference efficiency drops for $\Delta R < 0.2$. This is caused by the fact that the trigger muon reconstruction algorithms have problem to distinguish two muons that are too close. On the other hand, since the efficiency from the map was calculated under an assumption that the reconstruction efficiencies of the muons are uncorrelated, there is a clear discrepancy between the two methods for low values of ΔR. The opening angle is correlated to the momentum of the muons: the smaller angles mean larger momenta. For that reason the efficiency drops toward larger opening angles in the first plot and rise toward the larger value of q^2 in the second one.

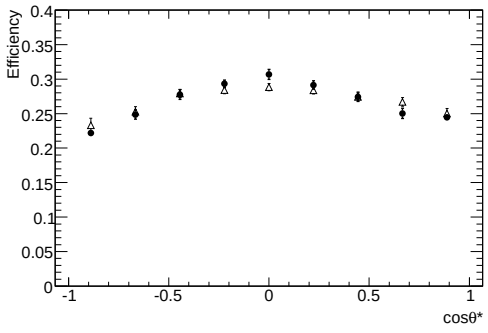

Figure 7.13: Efficiency of the di-muon trigger as a function of $\cos\theta^*$.

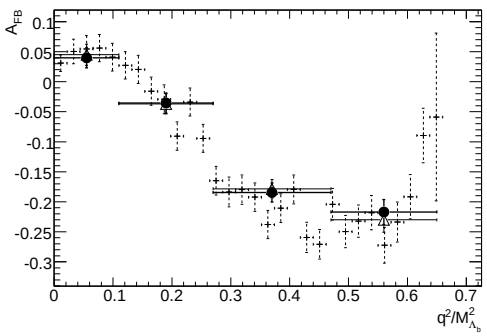

Figure 7.14: Forward-backward asymmetry for the generated sample (dashed crosses), after the di-muon trigger selection (open triangles) and after the emulation of the trigger using the map (solid circles).

Since we are investigating the forward-backward asymmetry, it is interesting

to look at a dependence of the efficiency on the decay angle $\cos\theta^*$. If this efficiency exhibits some asymmetry it will influence the results of the measurement. The efficiency is shown in Figure 7.13. It shows some asymmetry but the effect is tiny (in order of ~ 0.007). It is hard to tell whether this small asymmetry is caused by statistical errors or by the effect of p_{T} cut on the muons imposed by the trigger, as mentioned in Chapter 4.2. The problem is that when creating the plot we have effectively integrated over q^2 and thus the opposite-signed asymmetries in different q^2 regions cancelled.

Finally, the forward-backward asymmetry was calculated and it is shown in Figure 7.14. The asymmetry was calculated using the theoretical model implemented in the Monte Carlo generator (dashed crosses) and also using the true-matching reconstructed muons after the di-muon trigger selection. The latter ones were calculated as average values in four q^2 regions. In the real measurement the third region will be excluded since it contains the $\bar{\mathrm{c}}\mathrm{c}$ resonances. The di-muon trigger selection was made using the trigger decision (open triangles) and it was emulated using the trigger efficiency map (solid circles). Despite the systematic errors of the map, both sets of the values agree well and differences are safely within the statistical errors. However, we note that there is a visible discrepancy between the theoretical values and the ones after the trigger selection – the consequence of the p_{T} cuts.

The conclusion from these observations is that the forward-backward asymmetry is insensitive to the systematic errors caused by the finite binning of the map and by neglecting of the correlations between the single muon reconstruction efficiencies. However, it is sensitive to the trigger p_{T} cuts on the final state muons. Therefore, also this measurement requires the calibration of the di-muon trigger and this can be done using the tag-and-probe method with a sufficient precision.

We note that in this section we have studied only the influence of the di-muon part of the rare B decay trigger, even though the measured quantities can be influenced also by the hadronic part. The reason for that is that we don't have the trigger efficiency map for the inner detector tracking algorithms neither the method how to create it from the measured data.

Chapter 8

Conclusions

The algorithm for a trigger selection of the semimuonic rare B decays was developed. Its topological implementation was studied on $\Lambda_b \to \Lambda^0 \mu^+ \mu^-$ Monte Carlo sample and three different settings of the IDSCAN window size and the explicit a_0 cut were used (see Table 6.1). Apart from that, two different methods of Λ^0 reconstruction were used: the full and the partial reconstruction. Initial values of the selection cuts of the trigger algorithm were chosen using the distributions of true-matching tracks as 3σ range around the central values. Then the cut optimisation procedure was performed in order to achieve the best performance and to obtain a dependence of the maximal possible efficiency on the background rejection.

The efficiencies and the background rejection factors for the initial cut values are shown in Tables 6.2 and 6.3. The IDSCAN setting no. 1 gives worse results because of the explicit cut on a_0. The performance of the settings no. 2 and 3 is similar. The method with the partial Λ^0 reconstruction achieves much higher efficiencies than the full reconstruction method for 3σ cuts. However, the background rejection factors are correspondingly lower.

From the cut optimisation we have obtained the optimal efficiency as a function of the background rejection. The performance of the full and partial reconstruction method is similar for the low rejection factors ($< 90\%$), however the corresponding cuts for the full reconstruction method are not reasonable and there is a concern that they are over-trained for the given Monte Carlo sample. For the high rejection factors ($> 99\%$), the full reconstruction gives the results significantly better than the partial one gives. The cut optimisation plots are shown in Figure 6.10 and in Appendix A.

The background rate was estimated using $b\bar{b} \to \mu^+ \mu^- X$ Monte Carlo sample. We have reserved the level-2 output rate of 0.5 Hz for $\Lambda_b \to \Lambda^0 \mu^+ \mu^-$ channel and estimated the necessary background rejection to fill up this rate. The corresponding efficiencies for the different algorithm settings are shown in Table 6.5. Using the best setting, we have calculated the expected yield after three years of the initial luminosity run (integrated luminosity of 30 fb^{-1}) to be about 1900 signal events. Such a statistics corresponds to the one expected to be obtained

after the offline selection and allow us to distinguish (at CL of 1.6σ) between the standard model predictions of A_{FB} and the predictions of the models that differ by more than 8%.

The possibility of using the tag-and-probe method for the calibration of di-muon triggers was analysed as well as some possible sources of the systematic errors. The trigger efficiency map was constructed using $\mathrm{J}/\psi \to \mu^+\mu^-$ Monte Carlo sample.

The performance of the method was studied on J/ψ and Λ_b sample. The efficiency curves were created using either the trigger efficiency map or the trigger information from the sample. The curves created using both methods correspond within 7% except for some kinematical regions where the discrepancy is larger.

The usability of the trigger efficiency map for the trigger calibration was illustrated on two physics-motivated examples: the measurement of J/ψ polarisation and the measurement of the forward-backward asymmetry in $\Lambda_\mathrm{b} \to \Lambda^0\mu^+\mu^-$ process. We have shown that for both measurements, the systematic uncertainties of the map don't significantly affect the measured quantities.

References

[1] ATLAS Collaboration (1999): *ATLAS Detector and Physics Performance, Technical Design Report, Volumes I and II*, CERN/LHCC 99-14 and CERN/LHCC 99-15, CERN, Geneva

[2] ATLAS Collaboration (2003): *ATLAS High-Level Trigger Data Acquisition and Controls, Technical Design Report*, CERN/LHCC 2003-022, CERN, Geneva

[3] ATLAS Collaboration (1998): *ATLAS Level-1 Trigger, Technical Design Report*, ATLAS TDR–12, CERN, Geneva

[4] ATLAS Collaboration (1997): *ATLAS Inner Detector, Technical Design Report, Volumes I and II*, CERN/LHCC/97-16 and CERN/LHCC/97-17, CERN, Geneva

[5] ATLAS Collaboration (1997): *ATLAS Calorimeter Performance, Technical Design Report*, CERN/LHCC/96-40, CERN, Geneva

[6] ATLAS Collaboration (1997): *ATLAS Muon Spectrometer, Technical Design Report*, CERN/LHCC 97-22, CERN, Geneva

[7] ATLAS Collaboration (2008): *HLT Track Reconstruction Performance*, ATLAS-PUB-NOTE-2008, CERN, Geneva (in preparation), prepared by: W. Bell, E. Bouhova, M. Donega, M. Elsing, D. Froidevaux, G. Gorfine, S. Haywood, V. Kartvelishvili, T. Koffas, J. Lee, G. Piacquadio, T. Petersen, D. Price, C. Ruwiedel, A. Salzburger, L. Vacavant, J.-B. de Vivie, H. Zhu

[8] ATLAS Collaboration (2008): *Performance of the ATLAS Muon Trigger Slice with Simulated Data*, ATLAS-PUB-NOTE-2008, CERN, Geneva (in preparation)

[9] ATLAS Collaboration (2008): *Triggering on low-p_{T} muons and di-muons for B Physics*, ATLAS-PUB-NOTE-2008, CERN, Geneva (in preparation)

[10] ATLAS Collaboration (2008): *Heavy quarkonium physics with early ATLAS data*, ATLAS-PUB-NOTE-2008, CERN, Geneva (in preparation), prepared by: T. Alexopoulos, F. Antoniou, E. Etzion, E. N. Gazis, J. Ginzburg, V. Kartvelishvili, D. Price

[11] ATLAS Collaboration (2008): *Semileptonic Rare B-decays*, ATL-PHYS-PUB-2008, CERN, Geneva (in preparation), prepared by: C. Adorisio, G. Crosetti, Z. Dolezal, N. Nikitin, A. Policicchio, P. Reznicek, S. Sivoklokov, K. Toms

[12] T. Sjöstrand, S. Mrenna, P. Skands (2008): *PYTHIA 6.4 Physics and Manual*, FERMILAB-PUB-06-052-CD-T, Fermilab, Batavia

[13] A. Dewhurst, J. Ginzburg, V. Kartvelishvili, L. de Mora, D. Price, M. Smizanska, T. Stahl, W. Walkowiak (2007): *Low pT muon and di-muon rates in ATLAS*, ATL-COM-PHYS-2007-089, CERN, Geneva

[14] N. Nikitine, P. Reznicek, S. Sivoklokov, M. Smizanska and K. Toms (2007): *Potential of Rare B-decays in ATLAS*, Nuclear Physics B - Proceedings Supplements, Volume 163, January 2007, Pages 147-152

[15] N. Nikitin, F. Ohlson-Malek, P. Reznicek, S. Sivoklokov, L. Smirnova, M. Smizanska, K. Toms, S. Viret (2006): *Rare B-decays at ATLAS*, Nucl. Phys. B, Proc. Suppl. 156 (2006) 119-23

[16] P. Ball et al. (2000): *B Decays at the LHC*, CERN-TH/2000-101, CERN, Geneva

[17] Chuan-Hung Chena, C. Q. Geng (2001): *Baryonic Rare Decays of* $\Lambda_b \to \Lambda^0 \ell^+ \ell^-$, arXiv:hep-ph/0106193v1

[18] T. M. Aliev, K. Azizi, M. Savci (2007): *Analysis of rare* $B \to K_0^* \ell^+ \ell^-$ *decay within QCD sum rules*, arXiv:0710.1508v1

[19] CLEO Collaboration, G. Crawford et al. (1995): Phys. Rev. Lett. 75, 624 (1995)

[20] D. J. Lange (2001): *The EvtGen particle decay simulation package* Nuclear Instruments and Methods in Physics Research A 462 (2001) 152-155

[21] S. Alekhin et al. (2005): *HERA and the LHC: A Workshop on the implications of HERA for LHC physics*, Proceedings, Part B, CERN-2005-014, DESY-PROC-2005-01, Dec 2005, pages 315-415

[22] J. Allison (2007): *Geant4 - A Simulation Toolkit*, Nuclear Physics News, Volume 17 Issue 2, 20, Taylor & Francis

[23] Particle Data Group: Review of Particle Physics, *The European Physical Journal C* **3** (1998), 1 – 794

[24] R. Brun, F. Rademakers, P. Canal, I. Antcheva, D. Buskulic (2007): *ROOT An Object-Oriented Data Analysis Framework, User's Guide 5.16*, CERN e-book, http://root.cern.ch/root/doc/RootDoc.html

[25] R. Barlow (1997): *Statistics, A Guide to the Use of Statistical Methods in the Physical Sciences*, John Wiley & Sons

[26] P. Reznicek (2005): *Rare decay* $\Lambda_b^0 \to \Lambda^0 \mu\mu$, Slides from the talk given at ATLAS Physics Workshop, Rome

[27] ATLAS Collaboration (2006): *MuFast*, ATLAS twiki page, https://twiki.cern.ch/twiki/bin/view/Atlas/MuonHLTReviewLVL2muFast

[28] ATLAS Collaboration (2006): *Muon HLT Review*, ATLAS twiki page, https://twiki.cern.ch/twiki/bin/view/Atlas/MuonHLTReview

[29] ATLAS Collaboration (2006): *The ATLAS Computing Workbook*, ATLAS twiki page, https://twiki.cern.ch/twiki/bin/view/Atlas/WorkBook

Appendix A

Plots

Distributions of the true-matching track parameters

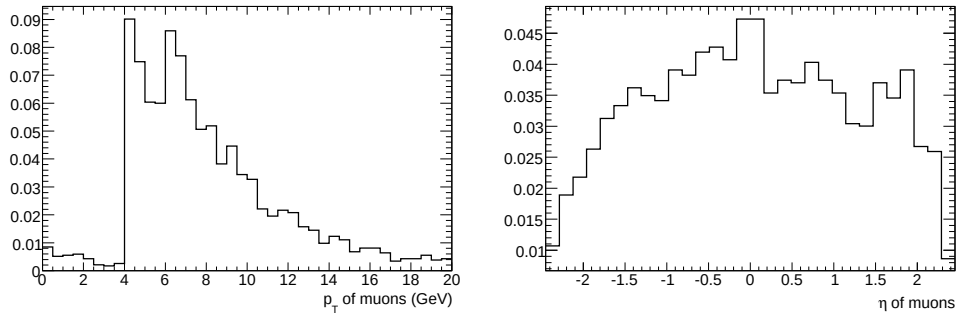

Distributions of the true transverse momentum p_{T} and pseudorapidity η of the final state muons in $\Lambda_{\mathrm{b}} \to \Lambda^0(p\pi)\mu^+\mu^-$ Monte Carlo sample.

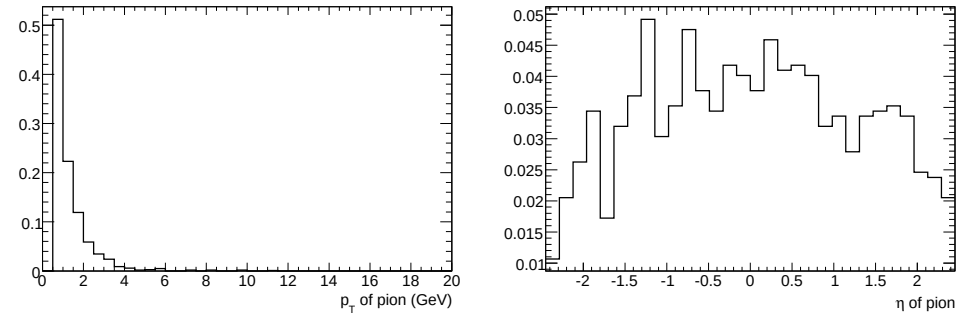

Distributions of the true p_{T} and η of the final state pion.

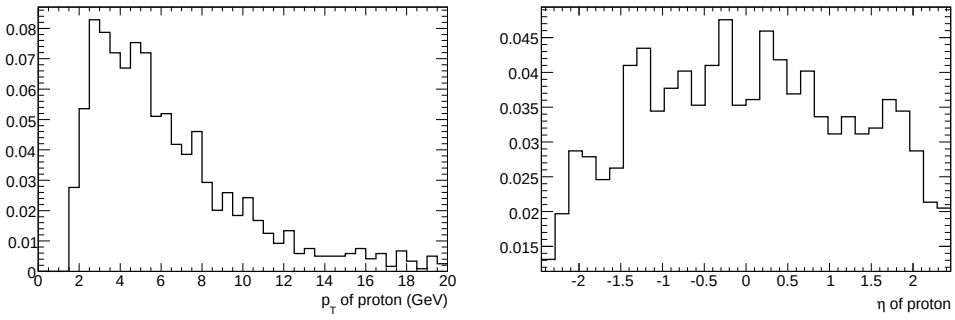

Distributions of the true p_{T} and η of the final state proton.

Hadronic final state reconstruction efficiencies

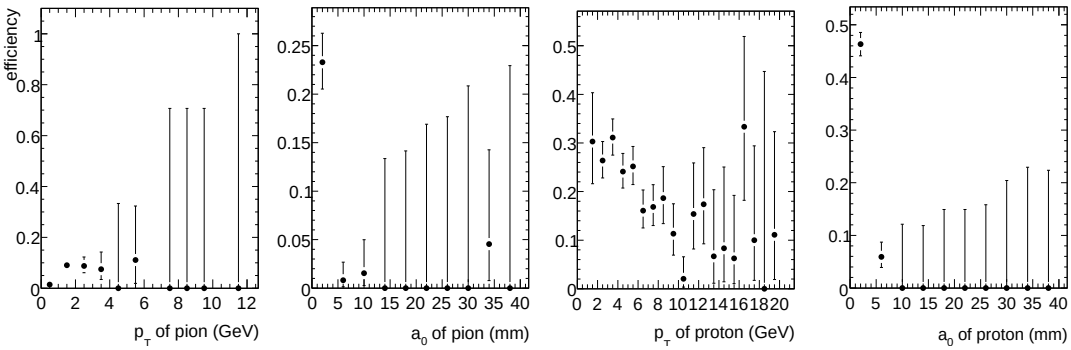

Level-2 reconstruction efficiency of the final state pion (two left plots) and proton (two right plots) of IDSCAN with the standard b-physics setting (setting no. 1).

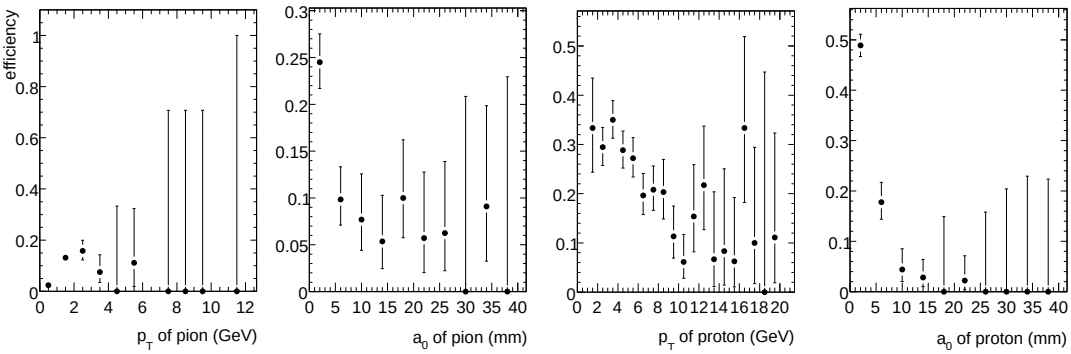

Level-2 reconstruction efficiency of the final state pion (two left plots) and proton (two right plots) of IDSCAN with the standard window size and loose a_0 cut (setting no. 2).

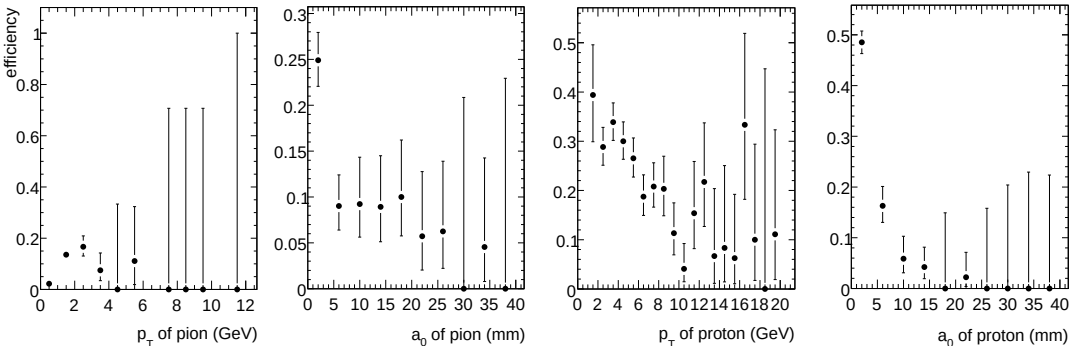

Level-2 reconstruction efficiency of the final state pion (two left plots) and proton (two right plots) of IDSCAN with the large window size and loose a_0 cut (setting no. 3).

Distributions of the true-matching track parameters

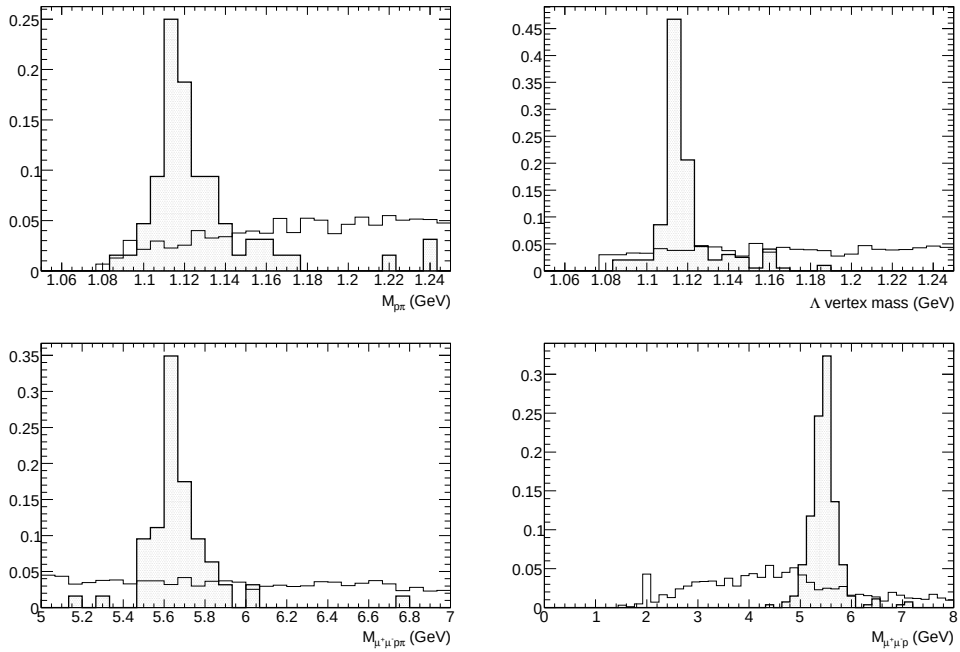

Distributions of Λ^0 mass before the vertexing (top left), Λ^0 mass after the vertexing (top right), the invariant mass of fully reconstructed Λ_b (bottom left) and the pseudo-mass of the partially reconstructed Λ_b (bottom right). The shaded histograms were made using the true-matching tracks while the open one were made using the background sample.

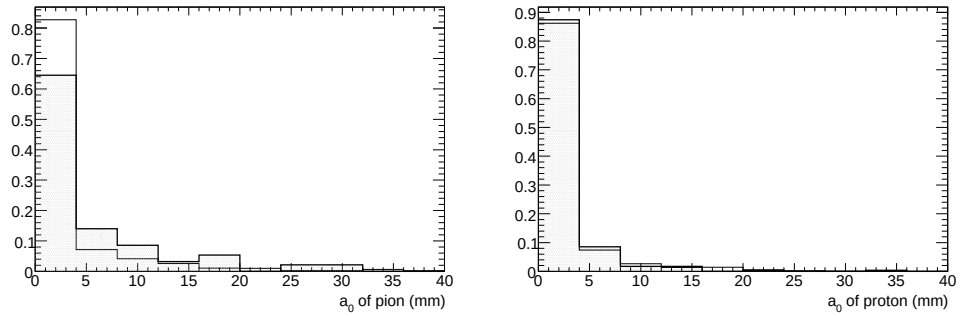

Distributions of a_0 of the pion (left) and the proton (right).

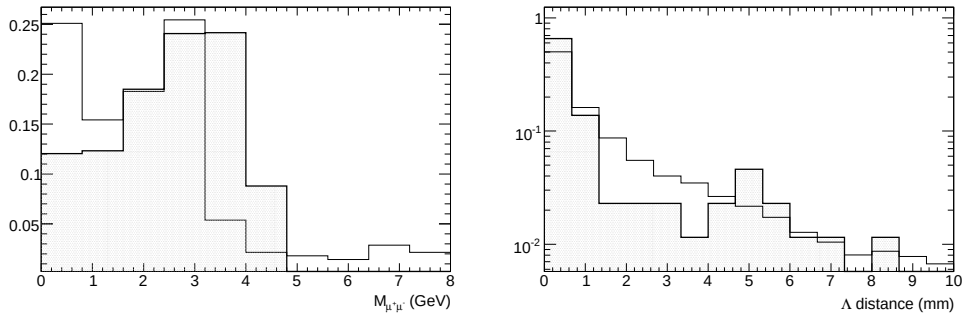

Distributions of the di-muon invariant mass (left) and Λ^0 track distance from the di-muon vertex (right).

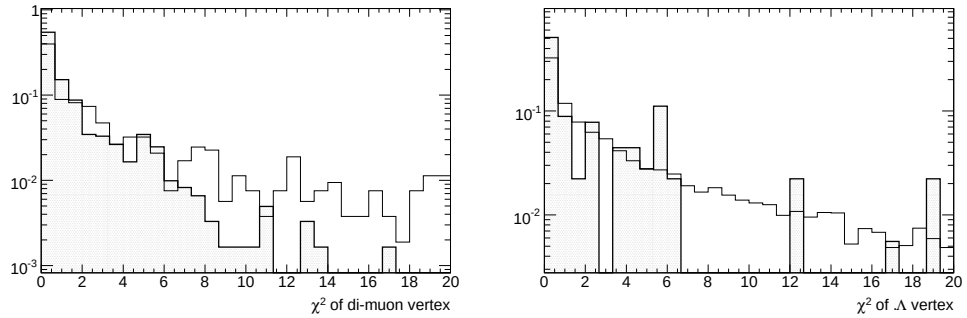

Distributions of the di-muon (left) and Λ^0 (right) vertex quality parameter.

Cut optimisation

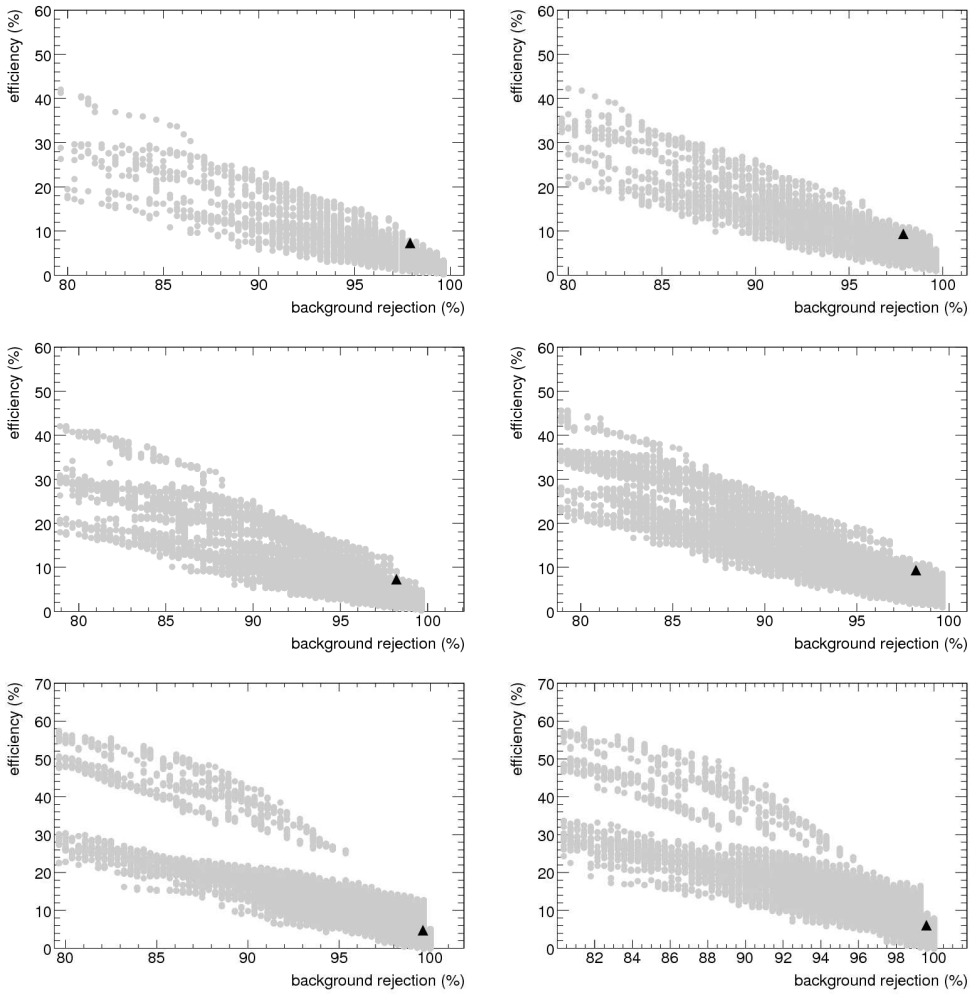

Results of the cut optimisation scan for the method with the full Λ^0 reconstruction. The plots in the first column are from the IDSCAN with the standard b-physics setting, the plots in the second column were made with the loose a_0 cut. The first row represents the method without vertexing, the second with the di-muon vertexing and the last one with the both vertexings.

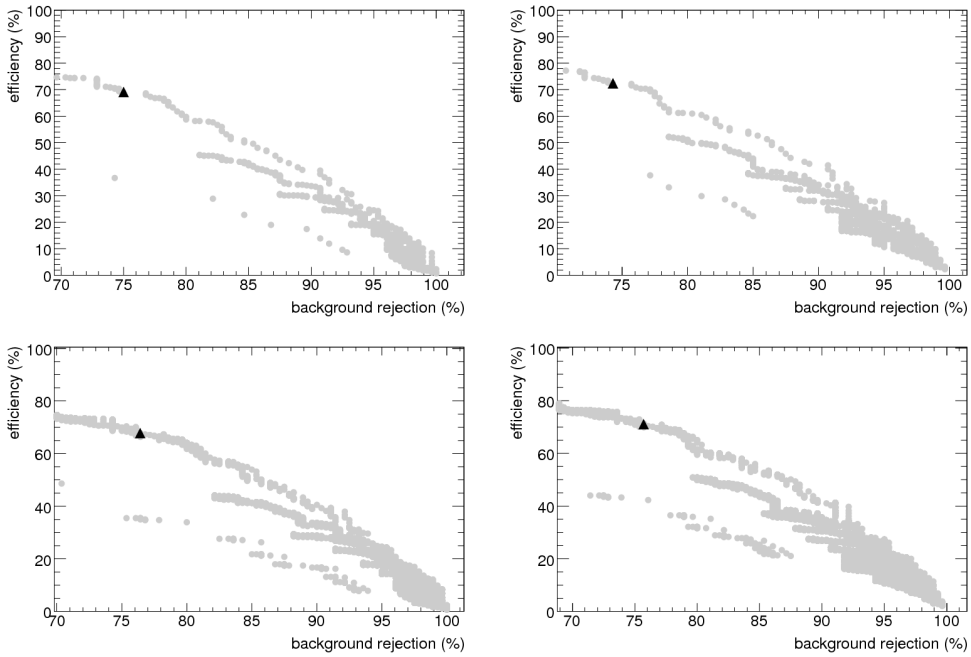

Results of the cut optimisation scan for the method with the partial Λ^0 reconstruction. The plots in the first column are from the IDSCAN with the standard b-physics setting, the plots in the second column were made with the loose a_0 cut. The first row represents the method without vertexing and the second with the di-muon vertexing.

Appendix B

Trigger Efficiency Map

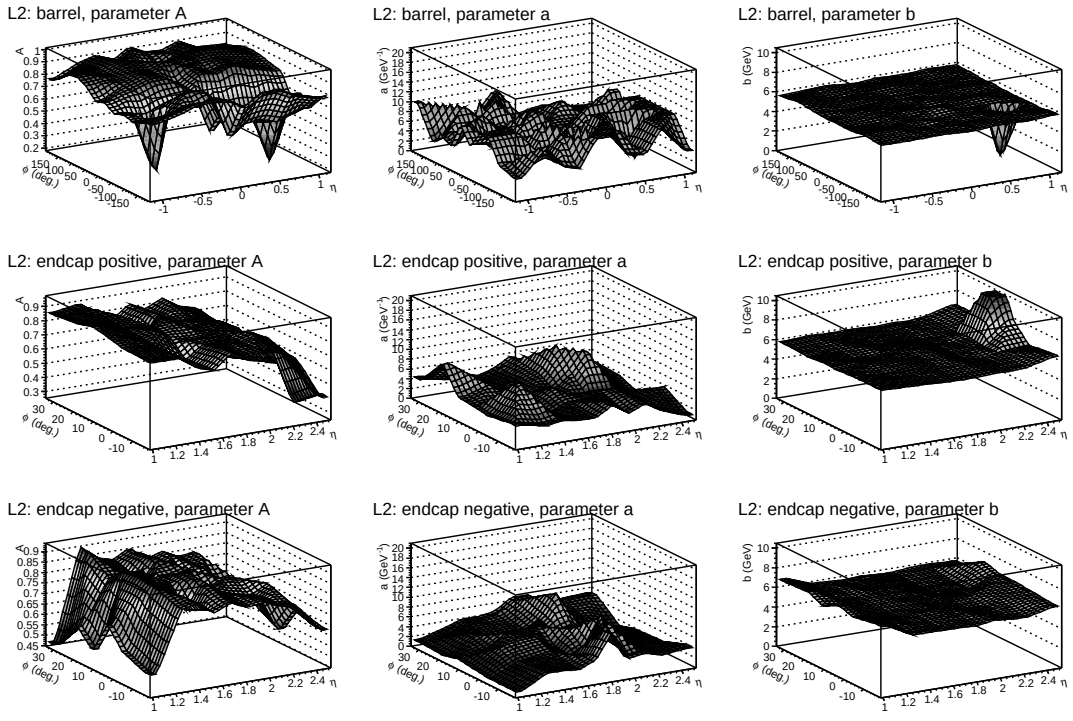

Trigger efficiency map. The first row shows values of the parameters A, a and b of Formula (7.9) as a function of η and ϕ in the barrel region. The second row shows the values for muon tracks with $q\eta > 0$ (q is charge) in the end-cap octant. The last row shows the values for $q\eta < 0$.